IMA Journal of Applied Mathematics (2026) , 1–30
https://doi.org/

Modelling the elastic entrance to plane-strain plastic sheet rolling

FRANCIS FLANAGAN
MACSI, Department of Mathematics & Statistics, University of Limerick, V94 T9PX, Ireland

MOZHDEH ERFANIAN AND EDWARD J. BRAMBLEY
Mathematics Institute and WMG, University of Warwick, Coventry, CV4 7AL, UK

ALISON N. O'CONNOR
CSIS and Lero, University of Limerick, V94 T9PX, Ireland

AND

DOIREANN O'KIELY*
MACSI, Department of Mathematics & Statistics, University of Limerick, V94 T9PX, Ireland
*Corresponding author: Doireann.OKiely@ul.ie

[]

When a sheet of elasto-plastic material is thinned by passing between two rollers, it first deforms elastically before subsequently deforming plastically. Here, the initial elastic deformation as the material enters the roll gap is modeled using two-dimensional (plane-strain) asymptotic analysis. For the first time, we find two distinct regimes informed by the yield strain. For small yield strains, typical of metals, the elastic deformation in the entrance is imposed by the plastically-deforming material in front of it. For larger yield strains, typical of plasticine which is often used for prototyping, the elastic deformation in the entrance is imposed by direct roller contact. Two asymptotic models are derived for these two regimes, a stress-forced model and a displacement-forced model, which are validated by comparison with elasto-plastic Finite Element simulations of the entire rolling process. The resulting models give physical understanding of the elastic entrance region, inform the entrance boundary conditions applied to existing models of plastic rolling, and highlight expected differences in behaviour between metal-forming processes and table-top lab-based experimental models of them using plasticine.

Keywords: mathematical modelling elastic deformation; asymptotic analysis; metal rolling; through-thickness.

1. Introduction

Sheet rolling is a process where a thick metal sheet is passed between two rollers, becoming longer and thinner as it travels through the "roll gap". Sheet rolling is an important step in metal forming, with over 99% of cast steel and two-thirds of wrought aluminium undergoing rolling as part of their processing (Allwood and Cullen, 2012, pp. 54–55). Deformation during rolling is primarily plastic, and mathematical models can be simplified significantly by neglecting elasticity. For example, Johnson (1991), Cawthorn et al. (2016) and Minton et al. (2016) all use a rigid–perfectly–plastic model, which gives a reasonable approximation of materials with minimal hardening and high elastic rigidity compared to the yield stress, such as lead, mild steel and some aluminium alloys. However, incorporating elastic-plastic material models does improve modelling of sheet rolling, and is essential for understanding changes in microstructure, mechanical properties and surface quality, as well as development of residual stress and downstream curvature (Lenard, 2013; Montmitonnet, 2006). Moreover, deformation is purely elastic when the material is below yield, which can occur in regions

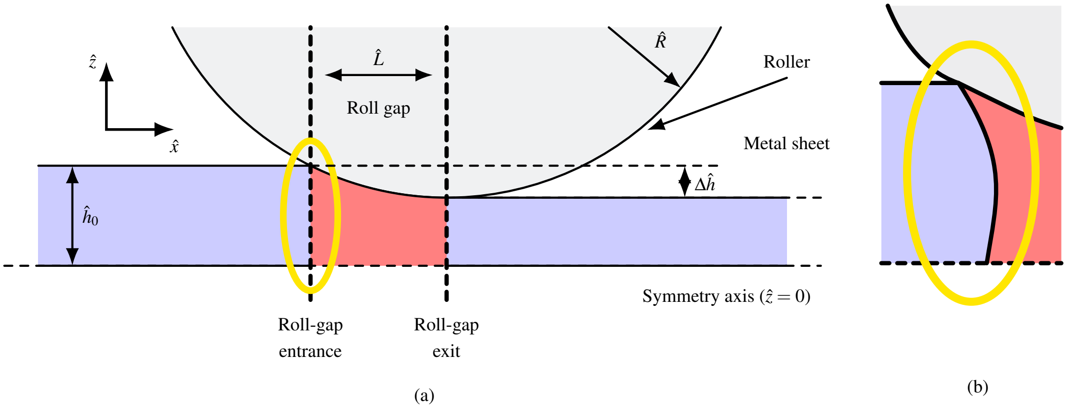

FIG. 1. A schematic of the rolling process. The blue regions are elastic deformation regions and the red is a plastic deformation zone. (b) shows a magnification of the entrance region from (a). The boundary between the blue elastic deformation region and the red plastic deformation region is not necessarily a straight vertical line. (Colour online)

near the start and end of the roll gap as well as outside the roll gap (Domanti and McElwain, 1995; Cherukuri et al., 1997; Cawthorn et al., 2016; Flanagan et al., 2025). For example, FE results presented in Cawthorn et al. (2016) suggest that the material they considered is sub-yield at the sheet surface for the first 20% of the roll gap, meaning that the strain there is elastic as opposed to plastic. Outside the roll gap, as a consequence of Saint-Venant's principle, plastic deformation in the roll bite promotes elastic stress fields extending on both sides of the roll bite of distances comparable with the strip width, typically meters (Montmitonnet, 2006). Additionally, recent work on modelling through-thickness variations in stress and strain distributions suggests that accurate prediction of through-thickness elastic stress and strain in a narrow elastic region at the roll-gap entrance is important for accurate prediction of through-thickness distributions inside and beyond the roll gap (Erfanian et al., 2025). Although these through-thickness variations may not have a significant impact on global quantities such as roll force and torque, they are an important factor in the development of residual stresses (Cherukuri et al., 1997; Flanagan et al., 2025).

In this paper, we use asymptotic analysis to study elastic behaviour in a metal sheet during rolling, focusing on the zone around the roll-gap entrance where stresses are significant but below yield, shown schematically in Figure 1. We assume that the yield stress of the material is small compared to the elastic modulus, so that strains at yield are small and linear elasticity can be assumed. We also assume there is both an elastic region and a plastic region in the small two-dimensional zone near the contact point, as illustrated in Figure 1b, separated by an initially unknown elastic–plastic boundary curve. Unlike slab models, the boundary curve is not necessarily a straight vertical line, and an accurate approximation of this boundary that separates the flowing and non-flowing regions is the key to solving such elastic-plastic problems (Howell et al., 2009). At the far left of the zone shown in Figure 1b, the influence of the rollers has diminished, leaving the material in a tension- and deformation-free state. At the far right of Figure 1b, the material is in full contact with the roll and deforms plastically. Thus, a non-zero solution in the elastic entrance region arises from forcing from the right, ensuring continuous stress and deformation, requiring knowledge of plastic behaviour to serve as the right-hand boundary condition of the region. A similar method is employed by Johnson (1987), where the rigid–perfectly–plastic zone from the entrance to the exit of a conical die is solved using the exit boundary condition, and the

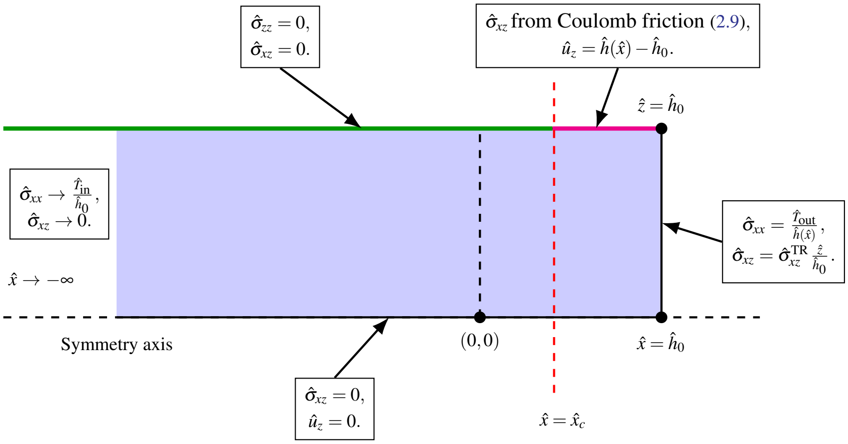

FIG. 2. Model D domain in dimensional form with boundary conditions. The contact $\hat{x}$-position between the sheet and the roller is $\hat{x}_c$, The green-coloured section of the top surface is the part of the sheet that is out of contact. The pink-coloured section is in contact with the roller. The boundary conditions are different for these sections of the domain. (Colour online)

resulting entrance boundary is then applied to the elastic entrance zone. However, this approach cannot be directly extended to rolling due to the complex surface friction conditions. For example, Erfanian et al. (2025) simplified the friction law to a Coulomb type and solved the stresses independently of velocities by assuming a prescribed boundary condition at the entrance. Instead, in the present study, we concern ourselves with only the entrance region, for which two possible two-dimensional reduced models are considered:

- Model D: A displacement-driven model where the elastic deformation in the entrance region is imposed by contact with the roller, and therefore variables are scaled based on the displacements imposed on the sheet by the roller.
- Model S: A stress-driven model where the elastic deformation in the entrance region is imposed by the stresses from the plastic deformation region, and therefore variables are scaled based on the magnitude of the stress components along the elastic–plastic boundary.

In Section 2, Model D is developed: elastic stresses are estimated for the entire entrance region, and an above-yield zone is estimated *a posteriori*. This model is compared to two separate FE simulations, and is shown to be more appropriate for modelling rolling of materials such as plasticine and to significantly overestimate the stresses in the entrance zone for metals typically used in rolling processes, such as steel. This motivates the alternative approach of Model S. Model S is then developed in Section 3; this assumes a parabolic form for the elastic–plastic boundary curve to facilitate model solution. This model is also compared to a FE model, and is found to predict the elastic stresses and displacements for steel much better than Model D does. Finally, conclusions are drawn in Section 4, as well as a discussion about potential improvements of the current entrance-region modelling.

2. Model D: displacement-driven

In this section, a displacement-driven model is formulated for the elastic entrance region at the start of the roll gap. The domain for this model is depicted in Figure 2; we initially work with dimensional variables, denoted with hats, before non-dimensionalising in Section 2.2 and identifying the small parameters to be exploited in the asymptotic analysis. We assume plane strain and consider a two-dimensional slice of the sheet that runs along the direction of rolling and across the sheet thickness as illustrated in Figure 2. We adopt Cartesian coordinates $\hat{\boldsymbol{x}} = (\hat{x}, \hat{z})$, with the x-axis along the sheet centreline and the $\hat{z}$-axis running across the sheet at the point where the roller would first contact the sheet if it was rigid-perfectly-plastic. The actual contact point is not known *a priori* because it depends on the elastic deformation of the sheet, and we anticipate it will be located in $\hat{x} > 0$. In principle the top surface of the sheet is curved due to the downward action of the roller, although the domain will simplify to a fixed rectangular shape in the limit of linear elasticity below. In the left region (coloured green in Figure 2), the surface of the sheet **is not** in contact with the top roller, and in the right region (coloured pink in Figure 2), the surface of the sheet **is** in contact with the top roller. Different boundary conditions will be applied in these two regions.

The right vertical ends of the domain are located at $\hat{x} = \hat{h}_0$, where $\hat{h}_0$ is the initial half-thickness of sheet. In the entrance zone, the stresses in the material increase rapidly as the sheet moves into the roll gap, and the limit of elasticity of the sheet is reached soon after entry, followed by permanent, plastic deformation (Lenard, 2013). We therefore truncate our elastic domain at $\hat{x} = \hat{h}_0$, with the expectation that the von Mises yield criterion is reached and elastic behaviour ceases before $\hat{x} = \hat{h}_0$. We will initially solve an elastic model on the whole domain depicted in Figure 2 and then check *a posteriori* where this breaks down; we also position the left-hand boundary sufficiently far to the left such that the predicted behaviour does not change significantly if we vary the exact location of the left-hand boundary. We denote the location where the elastically-deforming sheet and the roll first meet by $\hat{x}_{\mathrm{c}}$, and we expect $\hat{x}_{\mathrm{c}} \geq 0$. This contact $\hat{x}$-position is initially unknown, and must be set explicitly; the criterion for selecting the correct value of $\hat{x}_{\mathrm{c}}$ is outlined in Appendix A.

In the subsections below, the boundary conditions and the elasticity equations are explained. From the stress solution of this elasticity problem, we are able to determine the von Mises stress value at each spatial location in the domain. We use the von Mises values to loosely approximate the boundary $\hat{x}_{\mathrm{t}}$ between the elastic and plastic deformation zones. This means that we assume once the von Mises value reaches the yield stress, the theory of plasticity takes over and any elastic quantities obtained for $\hat{x}_{\mathrm{t}}(\hat{z}) < \hat{x} \leq \hat{h}_0$ should be disregarded. We acknowledge here that the plastic solution for $\hat{x} > \hat{x}_{\mathrm{t}}(\hat{z})$ would likely also have an influence in determining the stress and strain quantities in the elastic side of the entrance region, but since the plastic side of the full-thickness entrance region is beyond the scope of this work, here we will assume this influence is small and neglect it. All of these assumptions will be validated *a posteriori* by comparison with FE results in section 2.5.1.

2.1. *Boundary conditions for Model D*

Here, we work in the deformed (Eulerian) configuration, although since eventually displacements will be small this distinction will turn out not to matter unduly. On the left vertical end of the domain, we have a tension condition and a no-shear-stress condition

$$\hat{\sigma}_{xx} \to \frac{\hat{T}_{\mathrm{in}}}{\hat{h}_0}, \qquad \hat{\sigma}_{xz} \to 0, \qquad\qquad \text{as } \hat{x} \to -\infty, \tag{2.1}$$

where $\hat{\sigma}_{ij}$ are Cauchy stresses and $\hat{T}_{\mathrm{in}}$ is a tension per unit width applied to the far left of the domain in Figure 2 . We will see in Section 2.5 that the assumed shear condition at the far left agrees well with FE outputs.

Along $\hat{z}=0$ we have the symmetry conditions

$$\hat{u}_z = \hat{\sigma}_{xz} = 0, \qquad \text{at } \hat{z}=0, \tag{2.2}$$

where u_i denotes displacement in direction i.

At the right end of the domain, we prescribe a tension condition and a linearly-varying shear condition

$$\hat{\sigma}_{xx} = \frac{\hat{T}_{\text{out}}}{\hat{h}(\hat{x})}, \qquad \hat{\sigma}_{xz} = \hat{\sigma}_{xz}^{\text{TR}} \frac{\hat{z}}{\hat{h}_0}, \qquad \text{at } \hat{x}=\hat{h}_0, \tag{2.3}$$

where $\hat{T}_{\text{out}}$ is a tension per unit width applied to the far right of the domain and $\hat{\sigma}_{xz}^{\text{TR}}$ is the value of $\hat{\sigma}_{xz}$ at the top right corner of the domain, which is unknown but ultimately will not affect our leading-order analysis. For this model, we now set $\hat{T}_{\text{in}} = \hat{T}_{\text{out}} = 0$ for simplicity. In principle, we should impose some matching conditions at the right end of the domain to the plastic side of the entrance boundary layer. Since we do not know these conditions, as we are not solving for the plastic deformation here, and given that we do not know the exact location of the elastic–plastic boundary, we set a zero-tension condition for $\hat{\sigma}_{xx}$ and a linearly-varying condition for $\hat{\sigma}_{xz}$ at $\hat{x}=\hat{h}_0$. In FE results, $\hat{\sigma}_{xx}$ is approximately constant along $\hat{x}=\hat{h}_0$ and $\hat{\sigma}_{xz}$ varies approximately linearly in the $\hat{z}$-direction at $\hat{x}=\hat{h}_0$. This also allows the shear stress to simultaneously satisfy the boundary conditions at the top and bottom surfaces of the domain.

At the top surface of the domain that is out of contact (green section in Figure 2) the material is stress-free and so

$$\hat{\sigma}_{xz} = \hat{\sigma}_{zz} = 0, \qquad \text{at } \hat{z}=\hat{h}_0, \quad \text{for } \hat{x}<\hat{x}_c. \tag{2.4}$$

The boundary conditions along the in-contact part of the top surface (pink section in Figure 2) require a more detailed discussion, which is presented below.

At the top surface of the domain that is in contact (pink section in Figure 2), the material is displaced and sheared by the roller. The vertical displacement is determined by assuming the roller remains circular, giving the surface profile as

$$\hat{h}(\hat{x}) = \hat{R} + \hat{h}_0 - \Delta\hat{h} - \sqrt{\hat{R}^2 - (\hat{x}-\hat{L})^2}, \tag{2.5}$$

where $\hat{R}$ is the roll radius, $\Delta\hat{h} = \hat{h}(0) - \hat{h}(\hat{L})$ is the thickness change along the roll gap and $\hat{L} = \sqrt{2\hat{R}\Delta\hat{h} - \Delta\hat{h}^2}$ is the length of roll gap. Differentiating (2.5) with respect to $\hat{x}$, and evaluating at $\hat{x}=0$ because our focus is on the slope at the entrance region, we obtain

$$\hat{h}'(0) = \frac{-\hat{L}}{\sqrt{\hat{R}^2 - \hat{L}^2}} = \frac{-2\varepsilon r}{1-\varepsilon^2 r^2}, \tag{2.6}$$

where $\varepsilon = \hat{h}_0/\hat{L}$ is the roll-gap aspect ratio, $r = \Delta\hat{h}/\hat{h}_0$ is the reduction ratio and the last expression on the right-hand side is obtained by substituting for the roll radius $R = (\hat{L}^2 + \Delta\hat{h}^2)/2\Delta\hat{h}$. In cold rolling, $\varepsilon r \ll 1$; for example, Ghosh et al. (2004) cold roll the AA5049 alloy, with $\varepsilon r \approx 0.064$ for a 20% reduction.

We can use equation (2.5) to obtain an in-contact boundary condition for $\hat{u}_z$. A point on the roller surface has coordinate

$$\hat{z} = \hat{Z} + \hat{u}_z = \hat{h}(\hat{x}), \tag{2.7}$$

where $\hat{Z}$ is the undeformed (Lagrangian) position, here equal to $\hat{h}_0$ on the surface. Consequently, one of the conditions on the top surface of the domain that is in contact (pink section in Figure 2) is

$$\hat{u}_z = \hat{h}(\hat{x}) - \hat{h}_0 = \hat{R} - \Delta\hat{h} - \sqrt{\hat{R}^2 - (\hat{x} - \hat{L})^2} \qquad \text{at } \hat{z} = \hat{h}(\hat{x}), \quad \text{for } \hat{x} \geq \hat{x}_{\mathrm{c}}. \tag{2.8}$$

The other condition on the top surface of the domain in contact with the roller is Coulomb friction (characterised by the friction force being proportional to the normal force),

$$\hat{\sigma}_{xz}\left(1 - \left(\hat{h}'\right)^2\right) + \hat{h}'\left(\hat{\sigma}_{zz} - \hat{\sigma}_{xx}\right) = -\bar{\mu}\left[\hat{\sigma}_{zz} - 2\hat{\sigma}_{xz}\hat{h}' + \hat{\sigma}_{xx}\left(\hat{h}'\right)^2\right], \qquad \text{at } \hat{z} = \hat{h}(\hat{x}), \quad \text{for } \hat{x} \geq \hat{x}_{\mathrm{c}}, \tag{2.9}$$

where $\bar{\mu}$ is a constant friction coefficient. See Figure 2 for a visual description of the domain and boundary conditions.

2.2. *Dimensionless formulation for Model D*

To conduct asymptotic analysis, we take advantage of a small nondimensional parameter, and hence we must non-dimensionalise the governing equations and boundary conditions. The dimensional spatial variables, particularly $\hat{x}$, should be non-dimensionalised with $\hat{h}_0$ (and not $\hat{L}$) since we are concerned with a region of width $O(\hat{h}_0)$ near the entrance and not the full length of the roll gap. Since the slope of the sheet is $O(\varepsilon r)$ near $\hat{x} = 0$, it follows that the displacements are of $O(\varepsilon r \hat{h}_0)$, and hence we non-dimensionalise the displacements with $\varepsilon r \hat{h}_0$. We know the order of the displacements in this region, and hence we set the magnitude of the stress components based on these. For this reason, the stresses are non-dimensionalised with $\hat{E}\varepsilon r$, where $\hat{E}$ is the Young's modulus of the metal sheet, and this is why Model D is labelled as "displacement-driven". The full list of scalings are as follows:

$$\hat{x} = \hat{h}_0 x, \quad \hat{z} = \hat{h}_0 z, \quad \hat{\sigma}_{xx} = \hat{E}\varepsilon r \sigma_{xx}, \quad \hat{\sigma}_{zz} = \hat{E}\varepsilon r \sigma_{zz}, \tag{2.10a}$$

$$\hat{\sigma}_{xz} = \hat{E}\varepsilon r \sigma_{xz}, \quad \bar{\mu} = \varepsilon r \mu, \quad \hat{u}_x = \varepsilon r \hat{h}_0 u_x, \quad \hat{u}_z = \varepsilon r \hat{h}_0 u_z, \tag{2.10b}$$

$$\hat{x}_{\mathrm{c}} = \hat{h}_0 x_{\mathrm{c}}, \quad \hat{x}_{\mathrm{t}} = \hat{h}_0 x_{\mathrm{t}} \tag{2.10c}$$

$$\hat{h} = \hat{h}_0 h, \quad \Rightarrow \quad \hat{h}' = h'. \tag{2.10d}$$

The relevant small parameter for this asymptotic problem is therefore εr. Note that, since the Coulomb friction coefficient $\bar{\mu}$ is typically in practice small and of the same order of magnitude as εr, equation (2.10b) formalizes this by rescaling $\bar{\mu}$ by εr, and consequently we may think of μ as an order 1 quantity.

The relevant dimensional elasticity equations to be solved in the sheet are the reduced Cauchy momentum equations (steady-state, incompressible flow, and neglecting body forces) and the plane-strain Hooke's Law equations. Using the scalings described in equation (2.10), the governing equations may be written in non-dimensional form as

$$\frac{\partial \sigma_{xx}}{\partial x} + \frac{\partial \sigma_{xz}}{\partial z} = 0, \tag{2.11a}$$

$$\frac{\partial \sigma_{xz}}{\partial x} + \frac{\partial \sigma_{zz}}{\partial z} = 0, \tag{2.11b}$$

$$\frac{\partial u_x}{\partial x} = (1+\nu)\left[(1-\nu)\sigma_{xx} - \nu\sigma_{zz}\right], \tag{2.11c}$$

$$\frac{\partial u_z}{\partial z} = (1+\nu)\left[(1-\nu)\sigma_{zz} - \nu\sigma_{xx}\right], \tag{2.11d}$$

$$\frac{\partial u_x}{\partial z} + \frac{\partial u_z}{\partial x} = 2(1+\nu)\sigma_{xz}, \tag{2.11e}$$

where ν is the Poisson ratio. The boundary conditions (2.1)–(2.4), (2.8) and (2.9) become

$$
\begin{aligned}
&\sigma_{xx}, \sigma_{xz} \to 0, && \text{as } x \to -\infty, && (2.12a)\\
&\sigma_{xx} = 0,\ \sigma_{xz} = \varepsilon r A z, && \text{at } x = 1, && (2.12b)\\
&u_z = \sigma_{xz} = 0, && \text{at } z = 0, && (2.12c)\\
&\sigma_{xz} = \sigma_{zz} = 0, && \text{at } z = 1, \quad \text{for } x < x_c, && (2.12d)\\
&u_z = -2x + O\left(\varepsilon^2 r\right), && \text{at } z = h(x), \quad \text{for } x \geq x_c, && (2.12e)\\
&\sigma_{xz} + 2\varepsilon r(\sigma_{xx} - \sigma_{zz}) + \varepsilon r \mu \sigma_{zz} = O\left(\varepsilon^2 r^2\right), && \text{at } z = h(x), \quad \text{for } x \geq x_c, && (2.12f)
\end{aligned}
$$

where $A = (\sigma_{xz})_{\mathrm{TR}}/(\varepsilon r)$ (where $A = O(1)$ from (2.12f) owing to the scaling for μ assumed), and (2.6) can be used to simplify the dimensionless sheet surface shape as

$$h(x) = 1 - 2\varepsilon r x + O\left(\varepsilon^2 r\right), \quad \text{for } x \geq x_c \tag{2.13}$$

after taking the Taylor expansion about $x = 0$, leading to the u_z boundary condition in (2.12d).

2.3. *Leading-order solution for Model D*

To conduct an asymptotic analysis, an expansion is sought for each of the variables, σ_{xx}, σ_{zz}, σ_{xz}, u_x and u_z, of the form

$$P(x,z) = P^{(0)}(x,z) + \varepsilon r P^{(1)}(x,z) + \varepsilon^2 r^2 P^{(2)}(x,z) + O\left(\varepsilon^3 r^3\right). \tag{2.14}$$

We take the limit as $\varepsilon r \to 0$ and perform leading-order analysis. We can then write the leading-order formulation of the bulk equations (2.11) as

$$\frac{\partial \sigma_{xx}^{(0)}}{\partial x} + \frac{\partial \sigma_{xz}^{(0)}}{\partial z} = 0, \tag{2.15a}$$

$$\frac{\partial \sigma_{xz}^{(0)}}{\partial x} + \frac{\partial \sigma_{zz}^{(0)}}{\partial z} = 0, \tag{2.15b}$$

$$\frac{\partial u_x^{(0)}}{\partial x} = (1+\nu)\left[(1-\nu)\sigma_{xx}^{(0)} - \nu\sigma_{zz}^{(0)}\right], \tag{2.15c}$$

$$\frac{\partial u_z^{(0)}}{\partial z} = (1+\nu)\left[(1-\nu)\sigma_{zz}^{(0)} - \nu\sigma_{xx}^{(0)}\right], \tag{2.15d}$$

$$\frac{\partial u_x^{(0)}}{\partial z} + \frac{\partial u_z^{(0)}}{\partial x} = 2(1+\nu)\sigma_{xz}^{(0)}. \tag{2.15e}$$

The boundary conditions (2.12) at leading-order are simplified to

$$\sigma_{xx}^{(0)} = \sigma_{xz}^{(0)} = 0, \qquad \text{as } x \to -\infty, \tag{2.16a}$$

$$\sigma_{xx}^{(0)} = 0,\ \sigma_{xz}^{(0)} = 0, \qquad \text{at } x = 1, \tag{2.16b}$$

$$u_z^{(0)} = \sigma_{xz}^{(0)} = 0, \qquad \text{at } z = 0, \tag{2.16c}$$

$$\sigma_{xz}^{(0)} = \sigma_{zz}^{(0)} = 0, \qquad \text{at } z = 1, \quad \text{for } x < x_{\mathrm{c}}^{(0)}, \tag{2.16d}$$

$$u_z^{(0)} = -2x,\ \sigma_{xz}^{(0)} = 0, \qquad \text{at } z = 1, \quad \text{for } x \geq x_{\mathrm{c}}^{(0)}. \tag{2.16e}$$

Note the difference in boundary conditions between the $x < x_{\mathrm{c}}^{(0)}$ and the $x \geq x_{\mathrm{c}}^{(0)}$ sections of the top surface of the domain. Given the complexity of the mathematical formulation, an approximate solution technique is necessary.

2.4. *Numerical evaluation of Model D*

We solved (2.15), (2.16) numerically using fourth-order finite differencing[1]. The semi-infinite domain was truncated at $x = -2$ after verifying that increasing the domain size beyond this did not change the solution significantly. In a similar manner, the right-hand x-position was also chosen to be sufficiently large to ensure a reliable solution, and, as noted earlier, was set to $x = 1$.

We imposed both the bulk equations and boundary conditions on all boundaries, leading to an overdetermined system that was solved by finding the least-squares solution using MATLAB's `lsqminnorm` and `lsqr` functions. This was preferred over solving a square matrix system formed by dropping bulk equations at the boundaries, as this square matrix system was found to be ill-conditioned and consequently gave poor numerical accuracy. A convergence study showed that using a grid size of 801×2401 provides a sufficiently accurate finite-difference solution to the two-dimensional elastic entrance problem described by Model D, as described in Appendix A.

Finally, the leading-order contact x-position, $x_{\mathrm{c}}^{(0)} = 0.181$, was chosen by minimising the residual norm of the overdetermined system while ensuring the surface σ_{zz} stress remained smooth as the sheet enters the roll gap.

For a more in-depth description of the solution process, see Appendix A.

2.5. *Results of Model D and discussion*

In this section, we compare our findings from Model D with FE simulation results. Full details of simulations are described by Flanagan et al. (2025) so we give only a brief summary here. The simulations made in Abaqus/Standard with an implicit solver (Dassault Systémes, 2021). To comply with the plane-strain assumption, the sheet metal is modelled as a two-dimensional deformable part and the rolls as a two-dimensional analytical rigid geometry. The sheet has an initial full thickness $2\hat{h}_0 = 4\,\mathrm{mm}$, and the size and position of the rolls is such to give the required roll-gap aspect ratio $\varepsilon = 0.075$ and a reduction of $r = 0.25$. The contact between the roll and sheet is discretised using the surface-to-surface method with the friction coefficient of $\bar{\mu} = 0.1$. FE simulations are conducted for two different materials, brown plasticine and DC04 Steel, with the only difference between these

---

[1] A first attempt, using second-order-accurate finite differencing, led to leap-frogging behaviour, where the two "even" and "odd" x-derivatives are defined independently, and never affect each other, creating a repeating checkerboard pattern. Therefore, a fourth-order-accurate finite-difference scheme was employed to avoid leap-frogging.

TABLE 1 *Summary of FE simulation details used as comparisons against both elastic entrance-region models in this paper. The input parameters for the simulations are* ε*,* r *and* $\hat{Y}/\hat{E}$*, and* $x_{\mathrm{c}}^{\mathrm{FE}}$ *is an output.*

Sheet material	ε	r	$\hat{Y}/\hat{E}$	$x_{\mathrm{c}}^{\mathrm{FE}}$
Plasticine	0.075	0.25	0.03	0.148
DC04 steel	0.075	0.25	0.002	0.0166

simulations being their respective true stress–strain curves, and hence their $\hat{Y}/\hat{E}$ ratios, where $\hat{Y}$ is the initial yield stress and $\hat{E}$ is the Young's modulus of the material (see Table 1). The stress–strain curve defined for the brown plasticine is obtained from Sofuoglu and Rasty (2000), with $\hat{Y}/\hat{E} \approx 0.03$ and the curve for DC04 material is from Flanagan et al. (2025), with $\hat{Y}/\hat{E} \approx 0.002$. All those both ratios are much less than 1, the difference in order of magnitude will turn out to be significant below.

Plasticine, a wax-based modelling clay, is widely used for designing new metal-forming machines and control strategies prior to constructing full-scale systems, as its flow behaviour (yield and strain-rate hardening) can be calibrated to mimic warm or hot metal flow. Its applications in the literature range from simulating hot forging (Zhan et al., 2001; Bednarek et al., 2007; Hosseini-Ara and Yavari, 2018; Lee et al., 2015) to extrusion (Arentoft et al., 2000; Sofuoglu and Rasty, 2000) and hot-rolling processes (sheet (Fox and Sutcliffe, 2008; Buxton and Browning, 1972), ring (Stanistreet et al., 2006; Cleaver et al., 2016) and screw (Romantsev et al., 2018; Wójcik et al., 2021)). Having different $\hat{Y}/\hat{E}$ values, plasticine (representative of hot metal) and DC04 steel (in cold rolling) exhibit different behaviour when entering the deforming zone of the roll gap. In practice, $\hat{Y}/\hat{E}$ can be thought of as elastic strain at yield and therefore material with higher $\hat{Y}/\hat{E}$ can elastically strain much more before yielding. It will be shown that Model D produces results that agree well with the plasticine data, but is less accurate for typical cold-rolling metals. This motivates the formulation of a new elastic entrance-region model (Model S) tailored for cold-rolling metals. It should be noted that the applicability of the models is not restricted to the selected material, and the chosen materials serve only to illustrate the results.

2.5.1. Comparison against plasticine

Figures 3 and 4 compare stress and displacement components from Model D and the FE simulation for plasticine (see Table 1). The contour distributions are very similar. The contact point in the model is predicted to be $x_{\mathrm{c}}^{(0)} = 0.181$, which is relatively close to the value of $x_{\mathrm{c}}^{\mathrm{FE}} = 0.148$ from the FE simulation (calculated by determining where the first surface node with non-zero contact pressure is located). Using the scaling definitions from equation (2.10) and the values for plasticine steel in Table 1, we can express the von Mises criterion in dimensionless form to show that Model D predicts that plastic deformation takes over when

$$\sqrt{\frac{3}{4}(\sigma_{xx}-\sigma_{zz})^2+3\sigma_{xz}^2} = \frac{\hat{Y}}{\hat{E}\varepsilon r} \approx 1.59, \tag{2.17}$$

which means that our elasticity model is not valid for regions where the von Mises value is predicted to be greater than or equal to this value. The thick black contours in Figures 3a and 3b represent a dimensionless von Mises value of 1.59, and hence represent the elastic-plastic transition curves $x_{\mathrm{t}}(z)$. These $x_{\mathrm{t}}(z)$ curves are inside the roll gap for both the model and FE simulations.

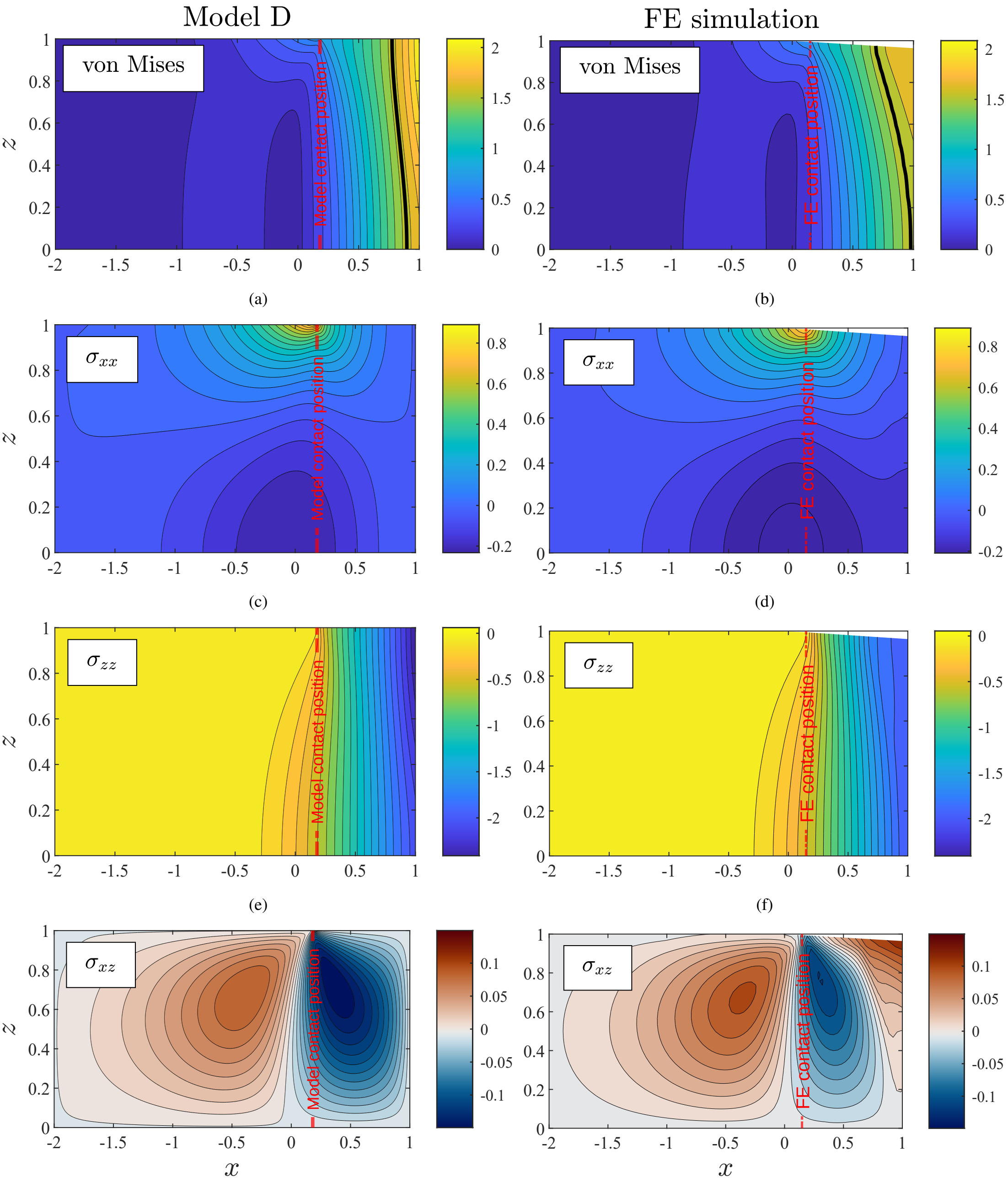

(a) (b) (c) (d) (e) (f) (g) (h)

FIG. 3. Dimensionless contour plots of von Mises stress (a,b), σ_{xx} (c,d), σ_{zz} (e,f), and σ_{xz} (g,h) results from the Model D elasticity solution (left) and the FE simulation (right) with parameters for brown plasticine material from Sofuoglu and Rasty (2000) (see Table 1). The thick black contours in (a,b) show where the sheet is predicted to begin plastically yielding. The model and FE contact points are $x_c^{(0)} = 0.181$ and $x_c^{\mathrm{FE}} = 0.148$, respectively. (Colour online)

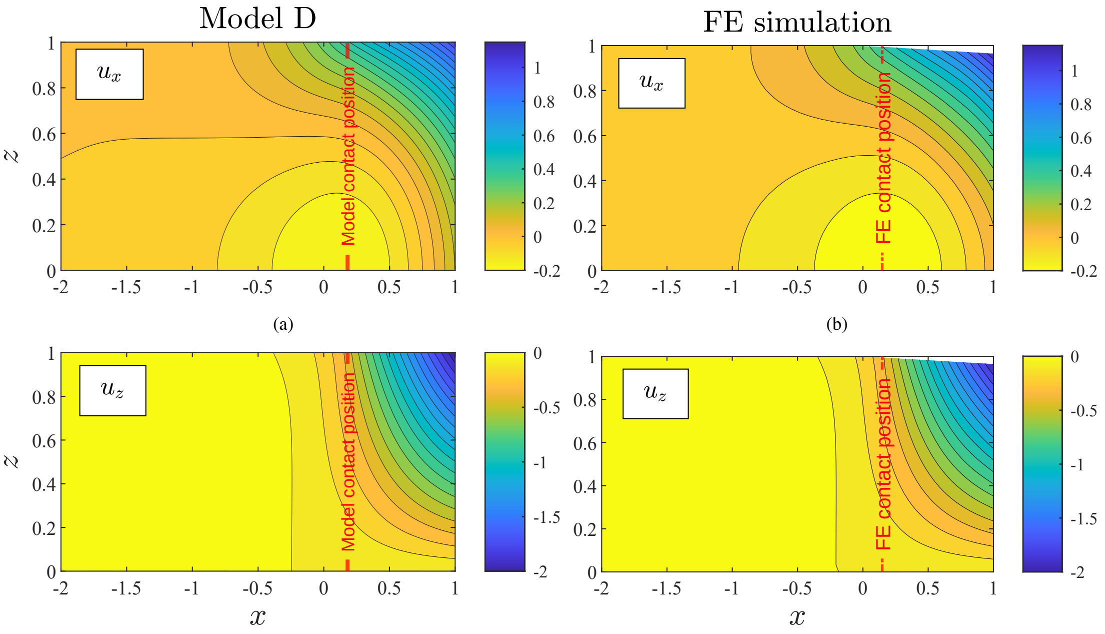

(a) (b)

(c) (d)

FIG. 4. Dimensionless contour plots of u_x (a,b) and u_z (c,d) from Model D elasticity solution (left) and the FE simulation (right) for brown plasticine material from Sofuoglu and Rasty (2000) (see Table 1). The model and FE contact points are $x_c^{(0)} = 0.181$ and $x_c^{\mathrm{FE}} = 0.148$, respectively. (Colour online)

The Model D results for σ_{xx} in Figure 3c are in good agreement with the FE results in Figure 3d. In both cases, the von Mises stress increases from 0 to yield as the material moves in the x-direction (Figure 3a,b). As the sheet deforms in contact with the roller, it experiences longitudinal tension near the the contact point ($\sigma_{xx} > 0$), with a corresponding region of longitudinal compression near the centreline of the sheet, below the contact point ($\sigma_{xx} < 0$). From the Model D and FE results, we note the dependence of σ_{xx} on both spatial variables, x and z. This two-dimensional elastic stress variation in both the rolling direction x and the through-thickness direction z is a feature that common slab-type methods lack in their analyses. In fact, most slab-type models assume rigidity in place of any elastic behaviour.

Figures 3e and 3f show the σ_{zz} solutions from the model and FE simulations, respectively. Once again we see reasonable agreement between the Model D output and the FE result. On the sheet's surface, the Model D normal stress varies quite smoothly from $\sigma_{zz}^{(0)} = 0$ to approximately $\sigma_{zz}^{(0)} = -2$ as x proceeds beyond the contact point. This is sensible as the contact stress is expected to be zero to the left of the contact point, and we expect $\sigma_{zz}^{(0)}$ to smoothly increase in magnitude as the roller smoothly contacts the sheet. The leading-order vertical stress does not vary significantly through the thickness of the sheet. As expected, the vertical stress magnitudes from the model and FE outputs begin to diverge past the elastic–plastic boundary, $x \geq x_t(z)$. This occurs because the elasticity model's governing equations are valid only up to the point where the von Mises criterion is satisfied (thick black contour in Figure 3a). In principle, elastic and plastic boundary-layer problems should be solved simultaneously to obtain an appropriate solution for all stress quantities, but the good agreement between FE and the

Model D output in the elastic region $x < x_t(z)$ validates the assumption that the influence of the plastic region on the elastic region in this case is minimal, and can therefore be neglected.

Figures 3g and 3h show the shear stress from the Model D and FE results respectively. Below the contact point, two shear lobes of opposite sign appear in both models. A third lobe appears in the plastic zone in the FE simulations; this is not predicted by Model D, which breaks down beyond yield. Based on the FE results at the roll-gap exit in Flanagan et al. (2025), we would expect that solving the two-dimensional reduced model elastic *exit* problem would yield similar lobes. However, a further boundary-layer analysis of the exit region would be necessary to determine the nature of the $\sigma_{xz}^{(0)}$ behaviour in that zone, which is outside the scope of this work.

Finally, Figure 4 compares the Model D and FE displacement results. In the least-squares approach followed to solve Model D, it is necessary to manually set an extra boundary condition of $u_x^{(0)} = 0$ at the bottom left corner of the domain ($x = -2,\ z = 0$) to reduce the degree of freedom of this variable. All displacement plots show relatively small amounts of deformation to the left of the contact point, as expected. Figure 4a shows the $u_z^{(0)} = -2x$ boundary condition is well-satisfied in this least-squares problem and the sheet deforms quite smoothly as it enters the roll gap. We see both x- and z-dependencies for each displacement variable, indicating that two-dimensional analysis is indeed necessary.

In summary, for rolling parameter regimes such that $\hat{Y}/\hat{E} = O(\varepsilon r)$ and with the thick black analytical contour as the right end of their region of applicability (representing the predicted $x_t(z)$ curve), the Model D elastic results compare well with the FE outputs, both qualitatively and quantitatively. In the following section, the application of Model D is tested for DC04 steel, a typical material in rolling processes, but with a $\hat{Y}/\hat{E}$ ratio much smaller than that of plasticine.

2.5.2. Comparison against DC04 steel

Stresses are presented in Figure 5 from both model (Model D) and the FE simulation for DC04 steel (see Table 1). There are two significant discrepancies between Model D and FE stress outputs. Firstly, although the stress results agree reasonably well in terms of the shapes of the contours, our model severely overestimates the stress magnitudes, and consequently misplaces the elastic–plastic boundary. In Model D, this boundary is taken as the initial location where the von Mises yield criterion is first satisfied by the calculated elastic stress components. The value of $\hat{Y}/\hat{E}\varepsilon r \approx 0.123$ for this comparison, and the thick black contours in Figures 5a and 5b represent this dimensionless value (and hence the elastic–plastic curve $x_t(z)$). The FE simulation predicts that yielding does not occur until after the contact point, whereas in our reduced model we see much higher von Mises values to the left of the contact point, showing the stress overestimation made by Model D. This overestimation is likely caused by an incorrect choice of the stress non-dimensionalisation factor in equation (2.10). In Model D, we chose the stress non-dimensionalisation factors based on the magnitude of the displacements. However, these results suggest that a more prudent approach might be to let the stresses govern the displacements, which is the route taken in Model S (see Section 3).

The second discrepancy between Model D and FE is associated with the contact point. The Model D contact point, $x_c = 0.181$, is much further away from $x = 0$ than the FE contact point, $x_c^{\mathrm{FE}} = 0.0166$. In Model D, the elastic strains are assumed to be of size εr, i.e., $\hat{Y}/\hat{E} = O(\varepsilon r)$. This allows for a significant amount of sheet elastic deformation to occur before the roller and the sheet actually come into contact, and the sheet is allowed to deform downwards at its surface, pushing the contact point further into the roll gap. However, this assumption does not apply to DC04 steel, for which $\hat{Y}/\hat{E} \ll O(\varepsilon r)$. In this case, elastic deformation is small in magnitude, and the elastic limit is reached shortly after entry.

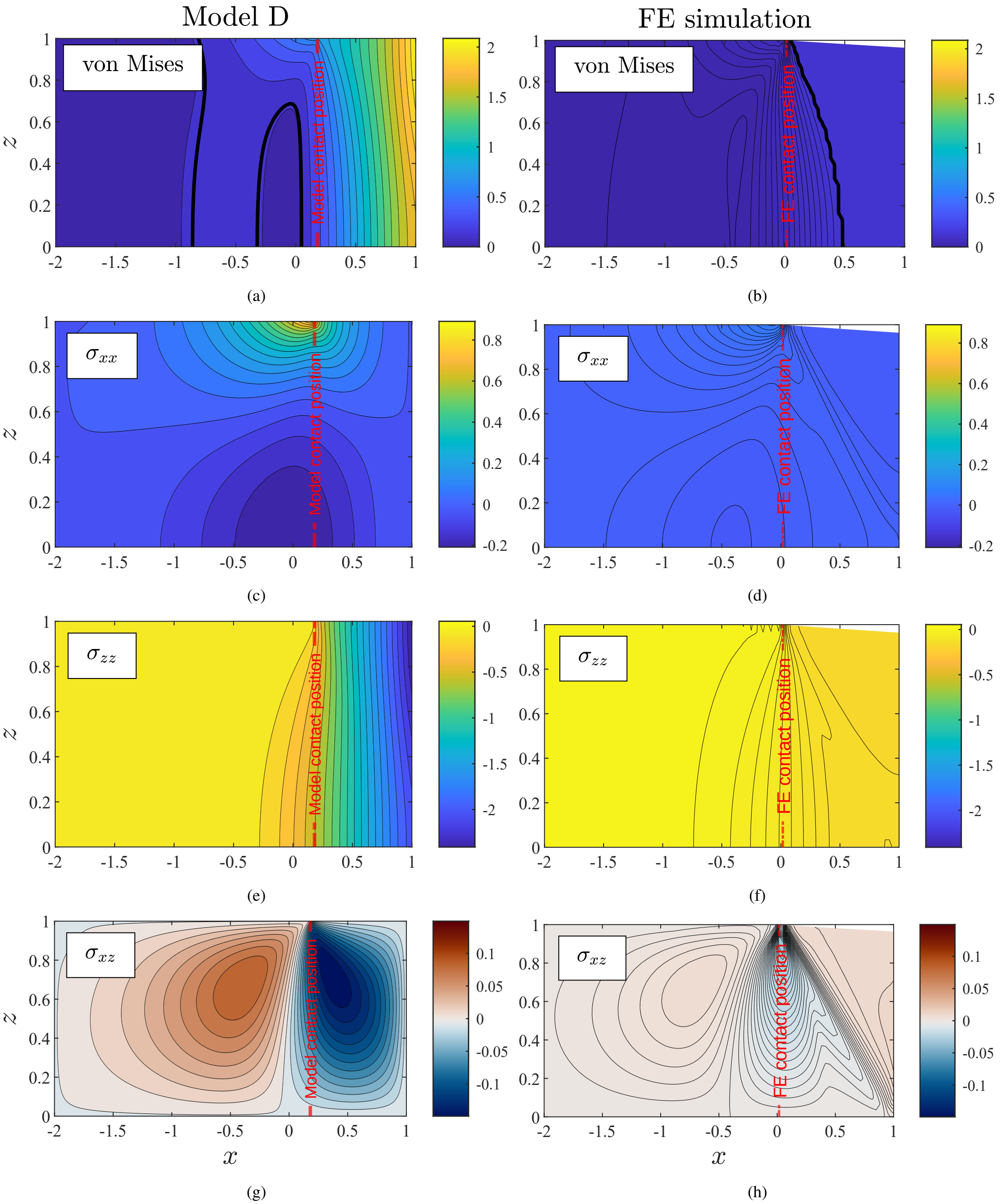

(a) (b)

(c) (d)

(e) (f)

(g) (h)

FIG. 5. Dimensionless contour plots of von Mises stress (a,b), σ_{xx} (c,d), σ_{zz} (e,f), and σ_{xz} (g,h) results from Model D elasticity solution (left) and the FE simulation (right) which employs the DC04 steel material (see Table 1). The thick black contours in (a,b) show where the sheet is predicted to begin plastically yielding. The model and FE contact points are $x_c^{(0)} = 0.181$ and $x_c^{\mathrm{FE}} = 0.0166$, respectively. (Colour online)

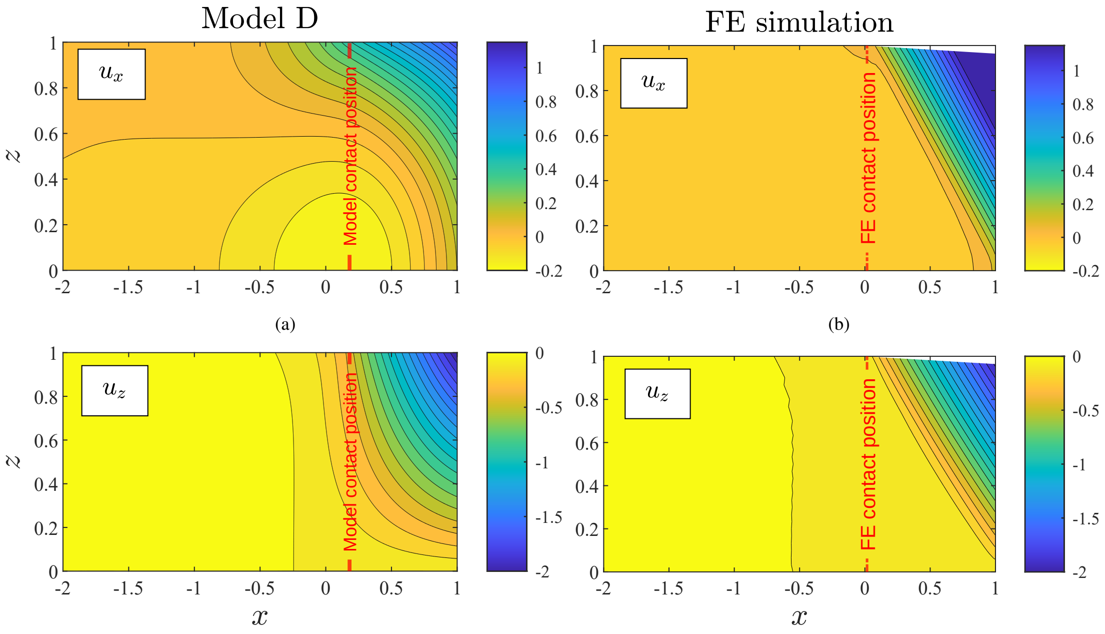

(a) (b)

(c) (d)

FIG. 6. Dimensionless contour plots of u_x (a,b) and u_z (c,d) from Model D elasticity solution (left) and the FE simulation (right) which employs the DC04 steel material (see Table 1). The model and FE contact points are $x_c^{(0)} = 0.181$ and $x_c^{\mathrm{FE}} = 0.0166$, respectively. (Colour online)

Consequently, as the FE shows, the sheet surface remains almost undeformed before contact, shifting the contact point closer to $x = 0$.

The displacements from both models are presented in Figure 6, and are qualitatively similar: increasing in magnitude both from left to right and from the centre to the surface of the sheet. The magnitude of the displacements are comparable and follow directly from boundary condition (2.16e), but the exact profiles predicted by the entrance-zone model differ markedly from the FE results. In particular, the FE displacements are approximately zero until the contact point, after which they appear to grow linearly in x and z, whereas the displacements predicted by Model D start to change before the contact point and do not follow a linear profile, indicating that Model D is not a good model for through-thickness displacement predictions during cold steel rolling. Therefore, we now discuss a second elastic entrance-region model, Model S, applicable to typical metals commonly processed by rolling for which $\hat{Y}/\hat{E} \ll O(\varepsilon r)$.

3. Model S: stress-driven

Model D was derived by assuming the magnitudes of the displacements in the entrance region were dictated by the intrusion of the roller into the sheet, and that this in turn set the size of the strains and elastic stresses. This model proved valid only for parameter regimes where $\hat{Y}/\hat{E} = O(\varepsilon r)$, as is typical of plasticine, for which a significant elastic region exists in contact with the roller (see Figure 3b). In contrast, for parameter regimes where $\hat{Y}/\hat{E} \ll O(\varepsilon r)$, as is typical in cold metal-rolling, the smaller

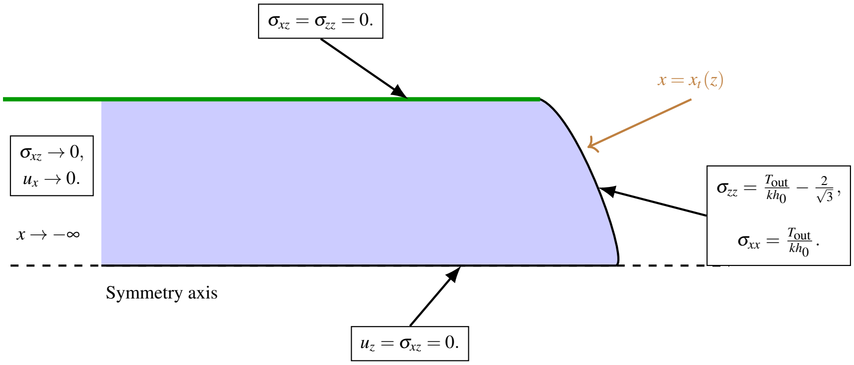

FIG. 7. Schematic of the Model S elastic entrance domain, with the dimensionless boundary conditions labelled along each boundary.

allowable elastic strains mean that there can only be a very small elastic zone in contact with the roller (as seen in Figure 5b). Therefore, defining a displacement boundary condition, as the one defined in Model D, is not useful; instead, information at the elastic–plastic boundary is required. Since the elastic–plastic boundary is defined by a stress condition, we now derive a stress-driven model, Model S, to contrast against the displacement-driven model Model D described above.

3.1. *Formulation for Model S*

As stated earlier, ideally, the elastic and plastic entrance-region problems would be solved simultaneously. Instead, here we assume in Model S that, for small $\hat{Y}/\hat{E}$, the initial contact point on the surface is the start of the $\hat{x}_{\rm t}(\hat{z})$ curve (i.e., $\hat{x}_{\rm t}(\hat{h}_0) = 0$). Based on the general shape of the elastic–plastic boundary in FE results (see, for example, the thick black contour in the FE von Mises result in Figure 5b), we approximate $\hat{x}_{\rm t}(\hat{z})$ as quadratic to leading order. Given the symmetric rolling problem under consideration, we expect $\hat{x}_{\rm t}(\hat{z})$ to be symmetric about $\hat{z} = 0$. We therefore assume that function $\hat{x}_{\rm t}(\hat{z})$ takes the form

$$\hat{x}_{\rm t}(\hat{z}) = \hat{x}_0\left(1 - \hat{z}^2/\hat{h}_0^2\right) + O\left(\hat{Y}/\hat{E}\right), \tag{3.1}$$

where $\hat{x}_0$ is the only remaining degree of freedom of the yielding boundary $\hat{x}_{\rm t}(\hat{z})$ in Model S to leading order, and gives the value of $\hat{x}_{\rm t}(0)$ on the symmetry axis $\hat{z} = 0$.

The yielding boundary now forms the right end of our dimensionless elastic entrance domain in Model S, as shown in Figure 7. Since we know that the von Mises criterion must be satisfied along the $\hat{x}_{\rm t}(\hat{z})$ curve, we can non-dimensionalise the entrance-region stress components with the yield stress $\hat{Y}$. We can then use this new stress non-dimensionalisation to obtain the appropriate displacement non-dimensionalisations that maintain the balance in the governing equations. We define new dimensionless variables, re-using un-hatted notation for convenience, via

$$\hat{x} = \hat{h}_0 x, \quad \hat{x}_\mathrm{c} = \hat{h}_0 x_\mathrm{c}, \quad \hat{x}_\mathrm{t} = \hat{h}_0 x_\mathrm{t}, \tag{3.2a}$$

$$\hat{z} = \hat{h}_0 z, \quad \hat{h} = \hat{h}_0 h, \quad \Rightarrow \quad \hat{h}' = h', \tag{3.2b}$$

$$\bar{\mu} = \varepsilon r \mu, \tag{3.2c}$$

$$\hat{\sigma}_{xx} = \hat{Y} \sigma_{xx}, \quad \hat{\sigma}_{zz} = \hat{Y} \sigma_{zz}, \quad \hat{\sigma}_{xz} = \hat{Y} \sigma_{xz}, \tag{3.2d}$$

$$\hat{u}_x = \frac{\hat{Y}}{\hat{E}} \hat{h}_0 u_x, \quad \hat{u}_z = \frac{\hat{Y}}{\hat{E}} \hat{h}_0 u_z. \tag{3.2e}$$

Here, scalings (3.2a)–(3.2c) are the same as we used for Model D, but scalings (3.2d)–(3.2e) are motivated by the adjacent plastic zone instead of the strains imposed by the roller inside the elastic zone. This is analogous to the scaling used elsewhere by Johnson (1987).

The dimensionless governing equations are

$$\frac{\partial \sigma_{xx}}{\partial x} + \frac{\partial \sigma_{xz}}{\partial z} = 0, \tag{3.3a}$$

$$\frac{\partial \sigma_{xz}}{\partial x} + \frac{\partial \sigma_{zz}}{\partial z} = 0, \tag{3.3b}$$

$$\frac{\partial u_x}{\partial x} = (1+\nu)\left[(1-\nu)\sigma_{xx} - \nu \sigma_{zz}\right], \tag{3.3c}$$

$$\frac{\partial u_z}{\partial z} = (1+\nu)\left[(1-\nu)\sigma_{zz} - \nu \sigma_{xx}\right], \tag{3.3d}$$

$$\frac{\partial u_x}{\partial z} + \frac{\partial u_z}{\partial x} = 2(1+\nu)\sigma_{xz}, \tag{3.3e}$$

in line with those used in Model D (cf. Equation 2.11). However, the domain and boundary conditions are now different as shown in Figure 7. These boundary conditions are

$$u_x, \sigma_{xz} \to 0, \qquad \text{as } x \to -\infty, \tag{3.4a}$$

$$\sigma_{xx} = \sigma_{zz} + \frac{2}{\sqrt{3}} = \frac{\hat{T}_\mathrm{out}}{\hat{Y}\hat{h}_0}, \qquad \text{at } x = x_\mathrm{t}(z), \tag{3.4b}$$

$$u_z = \sigma_{xz} = 0, \qquad \text{at } z = 0, \tag{3.4c}$$

$$\sigma_{xz} = \sigma_{zz} = 0, \qquad \text{at } z = 1. \tag{3.4d}$$

For the conditions (3.4b) on $x = x_\mathrm{t}(z)$, we first prescribe a normal stress σ_{xx}, where $\hat{T}_\mathrm{out}$ is a tension per unit width applied to the far right of the domain in Figure 7. We also assume that the material is at yield, and use the findings of Erfanian et al. (2025) to assume that $\sigma_{xz} \approx 0$; this then gives the stated condition for σ_{zz}. We note here that the non-zero stress along $x = x_\mathrm{t}(z)$ is forcing a non-zero solution, as opposed to a non-zero solution being forced by a non-zero displacement, as was the case with Model D. With $x_\mathrm{t}(z)$ prescribed it is possible to obtain a least-squares solution to this problem in a similar manner to the method used to solve Model D (see Appendix A for a detailed description of the least-squares solution process). Since the assumed elastic domain is not rectangular, we first make a change in variables and then solve the problem on a rectangular domain.

3.2. *Solution procedure*

Starting from the elastic-zone problem (3.3)–(3.4), assuming a boundary profile (3.1) and taking the limit $\hat{Y}/\hat{E} \to 0$ yields a closed problem that can be solved numerically. In this case, our asymptotic analysis corresponds to an expansion of the form

$$P(x,z) = P^{(0)}(x,z) + \big(\hat{Y}/\hat{E}\big)P^{(1)}(x,z) + \big(\hat{Y}^2/\hat{E}^2\big)P^{(2)}(x,z) + O\big(\hat{Y}^3/\hat{E}^3\big) \tag{3.5}$$

for dependent variables. We then simplify the numerical solution procedure by mapping

$$\zeta = x - x_{\mathrm{t}}(z), \qquad \phi = z \tag{3.6}$$

and solving on a regular domain $\zeta \in (-\infty, 0]$, $\phi \in [0,1]$.

For the solutions that follow, we set $\hat{T}_{\mathrm{out}} = 0$ to give the same zero-tension input condition as the FE numerics. The domain was trucated at $\zeta = -3$ and a fourth-order finite difference scheme applied with a mesh of size 801×2401. Further details, including the governing equations in the new coordinate system, can be found in Appendix A.4. Note that, for Model S, no contact x-position has to be chosen since we assume that the point $(x,z) = (0,1)$ is the top of the yielding boundary and the initial contact point (see Section 3 in the main text). However, we best-fitted the value of x_0 in (3.1) so that the assumed elastic–plastic curve $x_{\mathrm{t}}^{(0)}(z)$ best matched the FE results, finding $x_0 = 0.489$. Ideally, some alternative method would determine x_0 without the need for comparison with an FE simulation, perhaps by attempting to minimize $\sigma_{xz}^{(0)}$ at $\zeta = 0$, but our initial attempts to find such a method have not met with success, and so we leave this to future studies. Nonetheless, we hypothesise that $x_0 \approx 0.5$ will give adequate results for any parameter values provided $\hat{Y}/\hat{E}$ is small, since the only parameter that x_0 can depend on is $\hat{Y}/\hat{E}$.

3.3. *Results*

Model S results in Figures 8 and 9 are obtained by achieving a least-squares solution to the leading-order problem on the (ζ, ϕ) regular-grid domain with 801×2401 grid points, in the same way as for Model D, and then mapping back to (x,z) space (see Appendix A for details).

Comparison of Model S and FE for DC04 steel material is shown in Figure 8 for stress and in Figure 9 for displacement components. The Model S results are dimensionless and the FE results have been non-dimensionalised via equation (3.2). There is no data for $x > x_{\mathrm{t}}^{(0)}(z)$ in the Model S results since the limit of elasticity is assumed to have been exceeded in this region. Overall, Model S performs very well in terms of contour shapes and stress magnitudes up as far as $x = x_{\mathrm{t}}^{(0)}(z)$. In addition, the elastic displacements are seen to be in excellent agreement between the model and the FE results in Figure 9. We reiterate here that the value of x_0 used for the Model S results has been best-fitted to the FE simulation, and so such good agreement is not guaranteed for through-thickness elastic stress and strain predictions for every parameter regime. Nonetheless, fitting a single scalar parameter cannot be wholly responsible for the good agreement between Model S and FE, and so we have confidence in the correctness and applicability of this model and the assumptions behind it.

4. Conclusion

Asymptotic analysis is employed to develop two distinct two-dimensional elastic entrance-zone models for symmetrical rolling. In Model D, the elastic solution is forced by the displacement of the surface

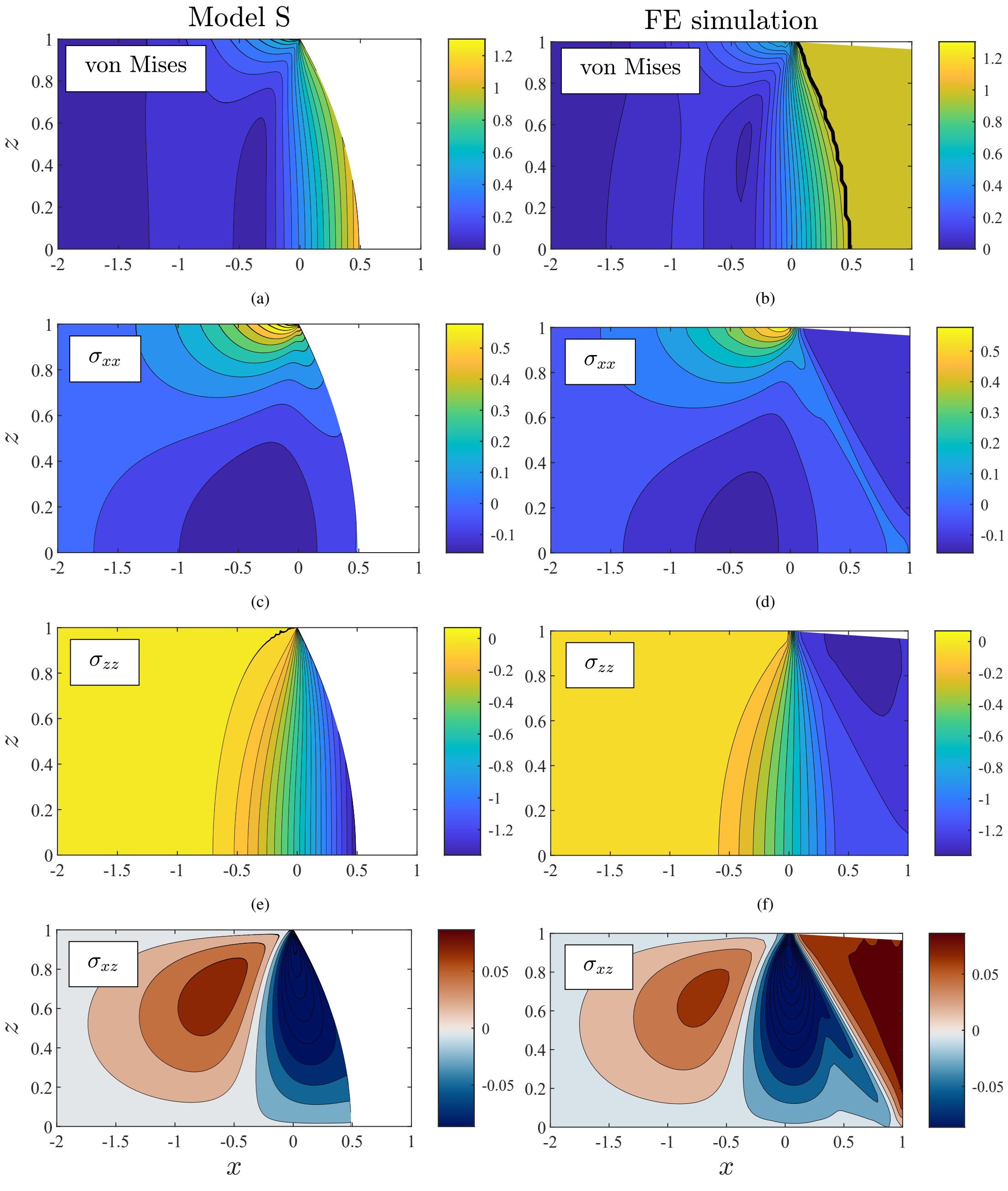

(a) (b)

(c) (d)

(e) (f)

(g) (h)

FIG. 8. Dimensionless contour plots of von Mises stress (a,b), σ_{xx} (c,d), σ_{zz} (e,f), and σ_{xz} (g,h) results from Model S elasticity solution (left) and the FE simulation (right) which employs the DC04 steel material (see Table 1). The thick black contour in (b) shows where the sheet is predicted to begin plastically yielding by the FE simulation. The Model S yielding boundary is the right end of the domain and is described by equation (3.1) with $x_0 = 0.489$. (Colour online)

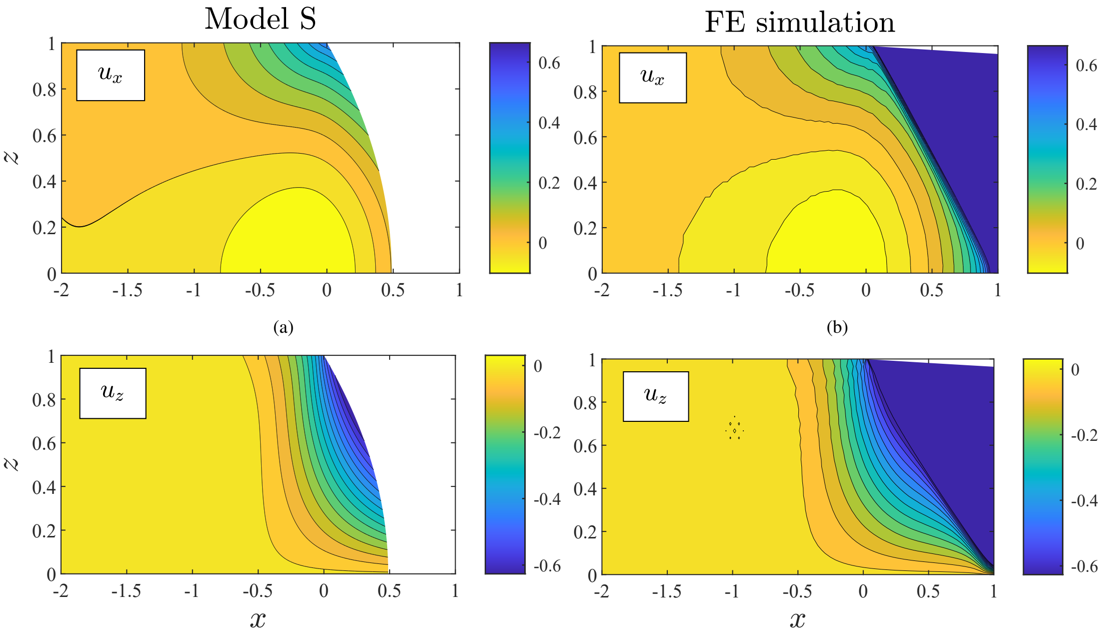

(a) (b)

(c) (d)

FIG. 9. Dimensionless contour plots of u_x (a,b) and u_z (c,d) from Model S elasticity solution (left) and the FE simulation (right) which employs the DC04 steel material (see Table 1). The Model S yielding boundary is the right end of the domain and is described by equation (3.1) with $x_0 = 0.489$. (Colour online)

by the roller, and the small parameter εr is utilised, where $\varepsilon = \hat{h}_0/\hat{L}$ is the roll-gap aspect ratio, and $r = \Delta\hat{h}/\hat{h}_0$ is the reduction ratio. In Model S, the elastic material does not contact the roller before it yields, and so the solution is forced by stresses from the plastic deformation region, and asymptotic analysis is based on the smallness of the yield strain $\hat{Y}/\hat{E}$. The Model D solution agrees well with FE simulations of plasticine but not steel, while the Model S solution does successfully reproduce the key features of FE simulations of steel. This demonstrates an important consequence of the present work: there are two different physical regimes, where, depending on the yield strain $\hat{Y}/\hat{E}$ of the material, two markedly different physical behaviours are seen as the material enters the roll gap.

Both models are solved numerically using a fourth-order-accurate finite-difference scheme, leading to an over-determined linear problem for which a least-squares solution is obtained. This method was found to be numerically robust, and a mesh sensitivity study ensures that sufficient mesh refinement is implemented.

One major reason for considering the elastic entrance region in the first place was to investigate the shape and nature of the elastic–plastic transition that happens at the beginning of the roll gap. In Model D, the contact x-coordinate where the sheet first contacts the roller, $x_c^{(0)}$, is selected to obtain a smooth result, with the elastic–plastic curve $x_t(z)$ then calculated by the model. In Model S, the contact x-coordinate is necessarily $x = 0$ at leading order, since for small $\hat{Y}/\hat{E}$ the strain can only be small before plasticity occurs. However, the elastic–plastic curve $x_t(z)$ takes an assumed form (here taken to be quadratic) rather than being calculated by the model, and one free parameter remains, $x_0 = x_t(0)$, which is here chosen to best fit to the FE results. Clearly, a method for calculating x_0 without recourse to FE results would constitute useful future work.

Both of the models have been derived as asymptotic models, valid provided some dimensionless parameter is small. Both models have only been expanded asymptotically to leading order in the small parameter; i.e. up to but not beyond the first non-zero term. While this should capture the dominant behaviour, it may miss smaller but still important features, such as the stress oscillations seen when modelling the plastic rolling region (Erfanian et al., 2025; Guo and Xiao, 2026). It is unclear whether expanding to higher orders would yield useful results, and this is left to future studies.

The two asymptotic models and the FE results all demonstrate significant through-thickness variation (as seen from figures 3, 4, 8 and 9, for example). This through-thickness variation is also seen in the plastic region, the elastic exit region, and the residual stress distribution post-rolling (Flanagan et al., 2025; Guo and Xiao, 2026), with recent success in modelling although only the first of these has been modelled asymptotically to date (Erfanian et al., 2025; Guo and Xiao, 2026). Through-thickness variation is often ignored for simplicity in slab-theory modelling, and is often under-resolved in FE simulations of rolling (Flanagan et al., 2025). The results presented here add weight to the argument that through-thickness variation should be understood and its important features carefully resolved. In practice, through-thickness variation cannot be detected from surface measurements such as roll force and roll torque, which are commonly used to validate models, but through-thickness variation is inherently important to through-thickness effects such as residual stress and flatness Guo and Xiao (2026).

The point at which the sheet first contacts the roller is mathematically important, as one of the boundary conditions suddenly changes at this point from a zero-normal-stress free-surface to a displacement-controlled no-penetration condition. Physically, one would not expect singular behaviour at this point, but instead a smooth transition without cusps in the sheet surface. In Model D, a smooth transition is indeed what the model predicts, provided the contact point $x_{\mathrm{c}}^{(0)}$ is chosen appropriately, and indeed this smooth transition gives a condition for finding $x_{\mathrm{c}}^{(0)}$. In Model S, however, the contact point at $x = 0$ is also the point at which the material transitions from elastic to plastic, and, in the plastic region, Erfanian et al. (2025) showed that this contact point is a singularity leading to an expansion fan of stress contours radiating out from this point; this is also seen here in both the elastic and plastic regions (for example, in Figure 8f). This has not been investigated further here. Future work could investigate this point further, either by considering an inner-asymptotic-region analysis very near the contact point, or by studying how Model S transitions into Model D as the yield strain $\hat{Y}/\hat{E}$ is increased.

Both of the models considered here attempt to investigate the elastic entrance region without needing to know the plastic solution beyond the entrance region. In practice, information from the plastic region may well impact the solution in the entrance region, just like the solution within the entrance region is needed to provide boundary conditions at the beginning of the plastic region (Erfanian et al., 2025). As mentioned above, it would of course be better to solve the full coupled elastic–plastic system, although this may not be tractable in any simplified or asymptotic model. Even if it were tractable, the models presented here have the advantage of being sufficiently simple to give physical understanding about the elastic entrance region, and even in the fully-coupled elastic–plastic case, it is likely that the distinction would remain between the displacement-forced and stress-forced cases. The investigation of fully-coupled elastic–plastic asymptotic modeling is left here to future studies.

Other future work could involve translating the elastic entrance modeling here into an elastic exit model, which would be important for predicting springback and residual stresses; an exit model would be complicated by the presence of significant plastic deformation in the governing equations. It may also be possible to generalize the model to an elastic–plastic model in the vicinity of the neutral point within the roll gap, where current plastic-only asymptotic modeling finds a plastic shock forming that is smoothed over in FE comparison simulations (Erfanian et al., 2025); an elastic–plastic inner model near the neutral point would help confirm whether this smoothness is due to the presence of elasticity. The effect of taking a non-zero entrance sheet tension $\hat{T}_{\mathrm{in}}$, which was here taken to be zero, could be studied; this would allow investigating how the elastic entrance region is altered during tandem rolling where there is tension between subsequent rolling stands. Finally, alternative or more complicated material models could be investigated to see what effect they have on the elastic entrance region; for example, anisotropy (perhaps due to preceding rolling or sheet processing), hardening, alternative yield criteria (e.g. Tresca), and sheet curvature could all be added to the models presented here. However, these additions would complicate the modelling presented in this paper, which may obscure the physical understanding presented here. In particular, the authors expect that the discovery of two distinct regimes (the steel rolling stress-forced regime of Model S and the plasticine rolling displacement-forced regime of Model D) is robust, and will not be altered significantly by including any of these extra complications.

Acknowledgements

ME gratefully acknowledges the support of a University of Warwick Chancellor's Scholarship. ME and EJB are grateful for the UKRI Future Leaders' Fellowship funding (MR/V02261X/1) supporting this work. FF is supported by Research Ireland Grant #18/CRT/6049. DOK is grateful for funding from the Research Ireland (21/FFP-P/10160). ANOC is supported by the European Union, Research Ireland and Lero, the Research Ireland Centre for Software, grants #101028291 and #13/RC/2094, respectively. For the purpose of open access, the authors have applied a Creative Commons Attribution (CC BY) licence to any Author Accepted Manuscript version arising from this submission.

REFERENCES

Julian M. Allwood and Jonathan M. Cullen. *Sustainable materials: with both eyes open*. UIT Cambridge, 2012. ISBN 978-1906860059. URL https://www.uselessgroup.org/publications/book/chapters.

Mogens Arentoft, Zbigniew Gronostajski, Adam Niechajowicz, and Tarras Wanheim. Physical and mathematical modelling of extrusion processes. *J. Mater. Process. Technol.*, 106(1-3):2–7, 2000. doi: 10.1016/S0924-0136(00)00629-4.

Sylwia Bednarek, Jan Sińczak, and Aneta Łukaszek-Sołek. Influence of height/diameter ratio of forging stock for variables of forging process of titanium alloy — physical and numerical modelling. *Obróbka Plastyczna Metali*, 18(3):31–37, 2007. URL https://bibliotekanauki.pl/articles/212090. (In Polish).

S. A. E. Buxton and S. C. Browning. Turn-up and turn-down in hot rolling: a study on a model mill using plasticine. *J. Mech. Eng. Sci.*, 14(4):245–254, 1972. doi: 10.1243/JMES_JOUR_1972_014_032_02.

C. J. Cawthorn, J. J. Minton, and E. J. Brambley. Asymptotic analysis of cold sandwich rolling. *Int. J. Mech. Sci.*, 106:184–193, 2016. doi: 10.1016/j.ijmecsci.2015.12.012.

H. P. Cherukuri, Robert E. Johnson, and R. E. Smelser. A rate-dependent model for hot-rolling. *Int. J. Mech. Sci.*, 39(6):705–727, 1997. doi: 10.1016/S0020-7403(97)81242-8.

Christopher J. Cleaver, Matthew R. Arthington, Sharareh Mortazavi, and Julian M. Allwood. Ring rolling with variable wall thickness. *CIRP Annals*, 65(1):281–284, 2016. doi: 10.1016/j.cirp.2016.04.002.

Dassault Systémes. SIMULIA User Assistance 2021 Abaqus, 2021. URL https://www.3ds.com/support/documentation/user-guides.

S. Domanti and D. L. S. McElwain. Two-dimensional plane strain rolling: an asymptotic approach to the estimation of inhomogeneous effects. *Int. J. Mech. Sci.*, 37(2):175–196, 1995. doi: 10.1016/0020-7403(94)00053-M.

Mozhdeh Erfanian, Edward J. Brambley, Francis Flanagan, Doireann O'Kiely, and Alison N. O'Connor. Through-thickness modelling of metal rolling using multiple-scales asymptotics. *Eur. J. Mech. A/Solids*, 113:105712, 2025. ISSN 0997-7538. doi: 10.1016/j.euromechsol.2025.105712.

Francis Flanagan, Alison N. O'Connor, Mozhdeh Erfanian, Omer Music, Edward J. Brambley, and Doireann O'Kiely. Through-thickness resolution, stress oscillations and residual stress in cold rolling. *Eur. J. Mech. A/Solids*, 114:105761, 2025. ISSN 0997-7538. doi: 10.1016/j.euromechsol.2025.105761.

M. N. Fox and M. P. F. Sutcliffe. Modelling material transfer in metal rolling using plasticine. *Wear*, 264(1-2): 18–25, 2008. doi: 10.1016/j.wear.2007.01.035.

S. Ghosh, M. Li, and D. Gardiner. A computational and experimental study of cold rolling of aluminum alloys with edge cracking. *J. Manuf. Sci. Eng.*, 126(1):74–82, 2004. doi: 10.1115/1.1645877.

Yunchang Guo and Hong Xiao. Investigation of rolling deformation oscillations and the bending mechanism in asymmetric rolling. *Journal of Materials Research and Technology*, 2026.

Reza Hosseini-Ara and Pouya Yavari. A new criterion for preform design of h-shaped hot die forging based on shape complexity factor. *International Journal of Material Forming*, 11(2):233–238, 2018. doi: 10.1007/s12289-017-1345-8.

Peter Howell, Gregory Kozyreff, and John Ockendon. *Applied Solid Mechanics*. Cambridge University Press, 2009. ISBN 978-0521671095.

Robert E. Johnson. Conical extrusion of a work-hardening material: an asymptotic analysis. *J. Eng. Math.*, 21(4): 295–329, 1987. doi: 10.1007/BF00132681.

Robert E. Johnson. Shape forming and lateral spread in sheet rolling. *Int. J. Mech. Sci.*, 33(6):449–469, 1991. doi: 10.1016/0020-7403(91)90081-D.

Sang-Jin Lee, Kyung-Hun Lee, and Byung-Min Kim. Design of roll profile for complex shape in shape rolling by combined 3D-EFA and BWT. *Int. J. Precis. Eng. Manuf.*, 16(2):281–286, 2015. doi: 10.1007/s12541-015-0037-x.

John G. Lenard. *Primer on flat rolling*. Elsevier, 2nd edition, 2013. ISBN 978-0080994185.

J. J. Minton, C. J. Cawthorn, and E. J. Brambley. Asymptotic analysis of asymmetric thin sheet rolling. *Int. J. Mech. Sci.*, 113:36–48, 2016. doi: 10.1016/j.ijmecsci.2016.03.024.

Pierre Montmitonnet. Hot and cold strip rolling processes. *Comput. Methods Appl. Mech. Eng.*, 195(48-49): 6604–6625, 2006. doi: 10.1016/j.cma.2005.10.014.

B. A. Romantsev, Tran Ba Huy, M. M. Skripalenko, M. N. Skripalenko, A. A. Gartvig, and Yu A. Gladkov. Investigation of the process of screw rolling in a four-roll stand by simulation. *Metallurgist*, 62(7):618–626, 2018. doi: 10.1007/s11015-018-0700-4.

Hasan Sofuoglu and Jahan Rasty. Flow behavior of plasticine used in physical modeling of metal forming processes. *Tribol. Int.*, 33(8):523–529, 2000. doi: 10.1016/S0301-679X(00)00092-X.

T. F. Stanistreet, J. M. Allwood, and A. M. Willoughby. The design of a flexible model ring rolling machine. *J. Mater. Process. Technol.*, 177(1-3):630–633, 2006. doi: 10.1016/j.jmatprotec.2006.03.228.

Łukasz Wójcik, Zbigniew Pater, Tomasz Bulzak, Janusz Tomczak, and Konrad Lis. A comparative analysis of the physical modelling of two methods of balls separation. *Materials*, 14(23), 2021. doi: 10.3390/ma14237126.

Mei Zhan, Yuli Liu, and He Yang. Physical modeling of the forging of a blade with a damper platform using plasticine. *J. Mater. Process. Technol.*, 117(1-2):62–65, 2001. doi: 10.1016/S0924-0136(01)01109-8.

A. Numerical Details

Finite differences are used to approximately solve both leading-order elastic entrance problems. Model D is solved on a regular grid in (x,z) space, while Model S requires a change of variables to (ζ,ϕ) space to be solved on a regular grid. The solution process is almost identical for both models, so we discuss the solution process for Model D only here for brevity, with a brief description of the subtle differences for the Model S case at the end (see Section A.4).

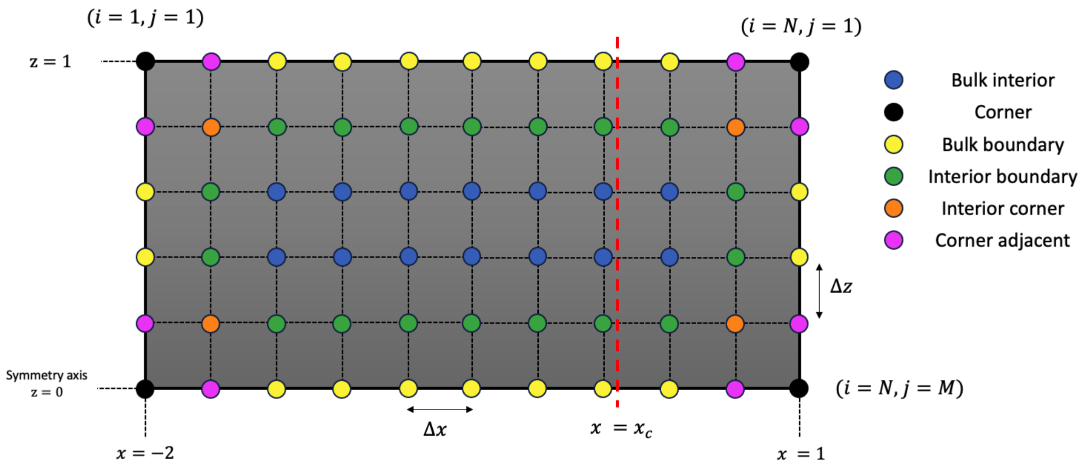

FIG. A.1. Discretised rectangular domain for the finite-difference solution of Model D. See Table A.2 for a description of the derivative approximations necessary at each mesh position.

The solution process for the elastic entrance Model D involves discretising the domain (see Figure A.1) and approximating the spatial derivatives in the problem with finite differences. The problem of solving five PDEs in five unknowns (three stress components and two displacement components) is thus reduced to a simple system of algebraic equations, $\mathsf{L}\boldsymbol{y} = \boldsymbol{b}$. The matrix L contains the left-hand side algebraic coefficients that define the approximations of the governing PDEs, along with the coefficients for the boundary conditions. The vector $\boldsymbol{b}$ contains the right-hand side values of those PDEs and boundary conditions. The desired solution vector $\boldsymbol{y}$ is initially unknown. Assuming we have M grid points in the z-direction and N in the x-direction, the first MN rows of $\boldsymbol{y}$ describe the solution of the quantity $\sigma_{xx}^{(0)}$ at each of the MN grid points, the next MN describe $\sigma_{zz}^{(0)}$, and so on. In total, this means that there will be $5MN$ rows in $\boldsymbol{y}$ and $5MN$ columns in L. If we require to satisfy the approximate form of each of the five PDEs at every grid point in the domain (see Figure A.1), then this gives $5MN$ simultaneous equations to solve, meaning that L would have $5MN$ rows. However, consideration must also be given to the boundary conditions along the edges of the domain. This leaves two options:

1. Define all of the boundary conditions in the problem by replacing a PDE approximation at a point with the boundary condition at that point; this means swapping a row of L that enforces a PDE with a row that enforces a boundary condition, and so maintains the square shape of L.
2. Define all five PDEs at every single grid point and all boundary conditions at every boundary point also; hence L will have more rows than columns leading to an overdetermined system of equations.

The first option is the most natural but leads to difficulties with obtaining a full-rank matrix for L, because there are ambiguities about which boundary conditions to implement in place of which equations. For this reason, the latter option is preferable here. We therefore seek a least-squares solution to the overdetermined system of algebraic equations $\mathsf{L}\boldsymbol{y} = \boldsymbol{b}$.

The domain we wish to solve on is unbounded as $x \to -\infty$ on the left (see Figure 2) For the finite-difference problem however, we obviously must define a numerical value at a finite x-position. Here we truncate the domain at $x = -2$ which we have ensured is sufficiently far enough away from $x = 0$ such that the solution is not influenced.

The first $5MN$ rows of L represent the coefficients for the five PDEs defined at each mesh point. For example, row 1 and row 2 of L contain the coefficients for the derivative approximations in the horizontal and vertical stress equilibrium equations respectively at mesh point $(i = 1, j = 1)$. Row 6 in matrix L corresponds to the horizontal stress equilibrium PDE but for position $(i = 1, j = 2)$, and so on. Rows $5MN + 1$ onwards of L contain the left-hand side coefficients for the boundary conditions for the leading-order problem, described in equation (2.16). The corresponding right-hand sides of these boundary conditions are stored in the vector $\boldsymbol{b}$. In fact, the $u_z^{(0)} = -2x$, $\sigma_{xx}^{(0)} = T_{\text{in}}$ and $\sigma_{xx}^{(0)} = T_{\text{out}}$ boundary conditions represent the only possibilities for non-zero entries in the vector $\boldsymbol{b}$ since the right-hand side of every other PDE and boundary condition is zero.

A.1. *Derivative approximations*

We discuss here the finite-difference derivative approximations used to approximately solve the leading-order equations in Model D. Second-order-accurate finite differencing led to leap-frogging behaviour. This leap-frogging behaviour occurs since in second-order central differencing, for example, the "even" x-derivative at point (i, j) is approximated based only on the values at points $(i-1, j)$ and $(i+1, j)$, and the "odd" derivative is approximated at point $(i+1, j)$ based only on the values at points (i, j) and $(i+2, j)$. This allows for locking to occur where the two "even" and "odd" x-derivatives are defined independently, and never affect each other, creating a repeating checkerboard pattern. Therefore, a fourth-order-accurate finite-difference scheme was employed, where the x-derivative at point (i, j) is now approximated based on the values at points $(i-2, j)$, $(i-1, j)$, $(i+1, j)$ and $(i+2, j)$, so no leap-frogging occurs.

The fourth-order-accurate derivative approximations used in different parts of the domain differ based on availability of mesh points above, below, to the left and to the right of the mesh point at which the derivative is being defined. The relevant finite-difference definitions used at each of the coloured mesh points in Figure A.1 are described in Table A.2. For example, the bulk interior points of the domain, (blue points in Figure A.1), require central differencing to approximate the derivatives in both x and z; at some general grid point (i, j) (with $3 \le i \le N-2$ and $3 \le j \le M-2$ to ensure the mesh point being considered is a bulk interior blue point) in the discretised domain in Figure A.1 with location (x_i, x_j), setting $f_{i,j} = f(x_i, z_j)$ as the value of the function f at the grid point, we have

$$\frac{\partial f}{\partial x}(x_i, z_j) \approx \frac{1}{\Delta x}\left[\frac{1}{12} f_{i-2,j} - \frac{2}{3} f_{i-1,j} + \frac{2}{3} f_{i+1,j} - \frac{1}{12} f_{i+2,j}\right], \tag{A.1a}$$

$$\frac{\partial f}{\partial z}(x_i, z_j) \approx \frac{1}{\Delta z}\left[\frac{1}{12} f_{i,j+2} - \frac{2}{3} f_{i,j+1} + \frac{2}{3} f_{i,j-1} - \frac{1}{12} f_{i,j-2}\right]. \tag{A.1b}$$

The relevant coefficients for each type of finite-difference derivative approximation are given in Table A.3. It is worth noting that the index j increases as z decreases, as shown in Figure A.1, and so the coefficients in the z-derivative terms are reversed compared to the x-derivative terms.

Using these derivative approximations, each PDE for each mesh point is written in the corresponding discretised algebraic form depending on the spatial location of the mesh point. It is then possible to obtain an approximate solution to the overdetermined system of algebraic equations, $\mathsf{L}\boldsymbol{y} = \boldsymbol{b}$.

TABLE A.2 *Types of derivatives needed at different spatial locations in the domain in Figure A.1.*

Grid point colour	**Label**	**Positioning**	**Derivative approximation**
Blue	Bulk interior	Internal point at least $2\Delta x$ or $2\Delta z$ away from a boundary	Central differencing for x and z derivatives
Black	Corner	Corner of domain	Forward/backward differencing is employed for both spatial derivatives
Yellow	Bulk boundary	Boundary point at least $2\Delta x$ or $2\Delta z$ away from a corner	Central differencing for either x or z derivative. Forward or backward differencing for the other spatial derivative
Green	Interior boundary	Internal point that is exactly Δx **or** Δz away from a boundary	Central differencing for either x or z derivative. Skewed forward or backward differencing for the other spatial derivative
Orange	Interior corner	Internal point that is exactly Δx **and** Δz away from a boundary	Skewed forward/backward differencing is employed for both spatial derivatives
Pink	Corner adjacent	Boundary point that is exactly Δx **or** Δz away from a corner	Forward/backward differencing is employed for one spatial derivative. Skewed forward/backward differencing is employed for the other spatial derivative

A.2. *Matlab implementation*

Figure A.2 provides an infographic of the procedure that is required to obtain a least-squares solution to the leading-order form of Model D. The first step in the process is to write all PDEs and boundary conditions in discretised form. The details of this step were discussed in Section A.1. The left-end x-position of the domain, $-\hat{d}/\hat{h}_0$ (here taken to be 2), and the contact x-position, x_c, should then be given explicitly.

Due to the division by the small quantities Δx or Δz in the derivative approximations, the weight of some equations in the least-squares minimisation problem is far greater than others. This is particularly problematic for boundary conditions as these contain no derivatives. The second step in our solution procedure re-weights our equations to ensure all PDEs and boundary conditions have roughly the same weight or importance in the minimisation problem. Each PDE at each mesh point is multiplied by $\Delta x \Delta z$. The boundary conditions are multiplied by Δx if they lie on a horizontal boundary and by Δz if they lie on a vertical boundary. This re-weighting ensures the largest term in each PDE and boundary condition is either $O(\Delta x)$ or $O(\Delta z)$ in order of magnitude. The number of mesh points in each spatial direction is chosen such that $\Delta x = \Delta z$. This gives each PDE and boundary condition similar weights and hence all

TABLE A.3 *Finite-difference coefficients for fourth-order-accurate derivative approximations. Column titles represent the number of mesh points away from the mesh point at which the derivative is being approximated. Each entry in the table represents a coefficient for a particular quantity in a finite-difference derivative approximation; blank entries are zeros.*

Type of differencing	−4	−3	−2	−1	0	1	2	3	4
Forward					−25/12	4	−3	4/3	−1/4
Skewed forward				−1/4	−5/6	3/2	−1/2	1/12	
Central			1/12	−2/3		2/3	−1/12		
Skewed backward		−1/12	1/2	−3/2	5/6	1/4			
Backward	1/4	−4/3	3	−4	25/12				

of these equations are more likely to be well-satisfied in the minimisation problem. A diagonal matrix called R applies the re-weightings and we now seek a solution to the system $\mathsf{RL}\boldsymbol{y} = \mathsf{R}\boldsymbol{b}$ instead of $\mathsf{L}\boldsymbol{y} = \boldsymbol{b}$.

The third step in the procedure described in Figure A.2 involves explicitly making the matrix L and the vector $\boldsymbol{b}$. The relevant variable coefficients in the relevant rows for each PDE and boundary condition are assembled in the matrix L and the corresponding right-hand side values of the PDEs and boundary conditions are inserted in the correct positions of the vector $\boldsymbol{b}$. It is then possible to use the built-in least-squares solver `lsqminnorm` to obtain a least-squares solution for the vector $\boldsymbol{y}$ on a relatively coarse mesh. This solver returns a vector $\boldsymbol{y}$ that approximately solves the system of linear equations $\mathsf{RL}\boldsymbol{y} = \mathsf{R}\boldsymbol{b}$ by minimising the value of $||\mathsf{RL}\boldsymbol{y} - \mathsf{R}\boldsymbol{b}||$. If several solutions exist to this problem, then `lsqminnorm` returns the solution that minimises $||\boldsymbol{y}||$. However, since the matrix L has to be assembled directly for this method, memory requirements cap the finite-difference mesh size, and the resolution of the numerical solution is quite low. The solution from the `lsqminnorm` solver is therefore interpolated onto a much finer finite-difference grid. This interpolated quantity is labelled $\boldsymbol{y}_0$. This makes up the fourth step in our solution procedure.

The final step in Figure A.2 is to use $\boldsymbol{y}_0$ as the initial guess for the built-in iterative MATLAB least-squares solver called `lsqr`. This solver allows the input for the coefficient matrix to be a matrix or a function handle. To use the function handle, the written function must be capable of returning the matrix-vector products $\mathsf{RL}\boldsymbol{y}$ and $\mathsf{L}^T\mathsf{R}\boldsymbol{z}$, where $\boldsymbol{z}$ is an arbitrary vector with the same number of rows as L. This function script is used as the input for the `lsqr` solver. The benefit of this solution technique as opposed to the `lsqminnorm` solver is that it allows for much finer resolutions because the matrix L does not have to be made directly using this method. A right-hand side vector is still required as an input, and so the vector $\mathsf{R}\boldsymbol{b}$ is used. This solver iterates until some tolerance (default value of 10^{-6} in this case) is met.

Although the `lsqr` solver would converge for any initial guess, the chosen technique is to use $\boldsymbol{y}_0$ as the initial guess to save CPU time. The first solution procedure using the `lsqminnorm` solver is used to obtain a solution on a relatively coarse mesh (51×151), and this is interpolated onto a finer mesh grid. This interpolated solution is used as an initial guess for the `lsqr` solver method. A brief convergence study showed 801×2401 to be a sufficiently refined finite-difference grid size. Figure A.3 gives a visual description of this convergence study. For each stress or displacement quantity, a larger-grid-size solution (with roughly double the number of grid points) is downsized to the preceding grid

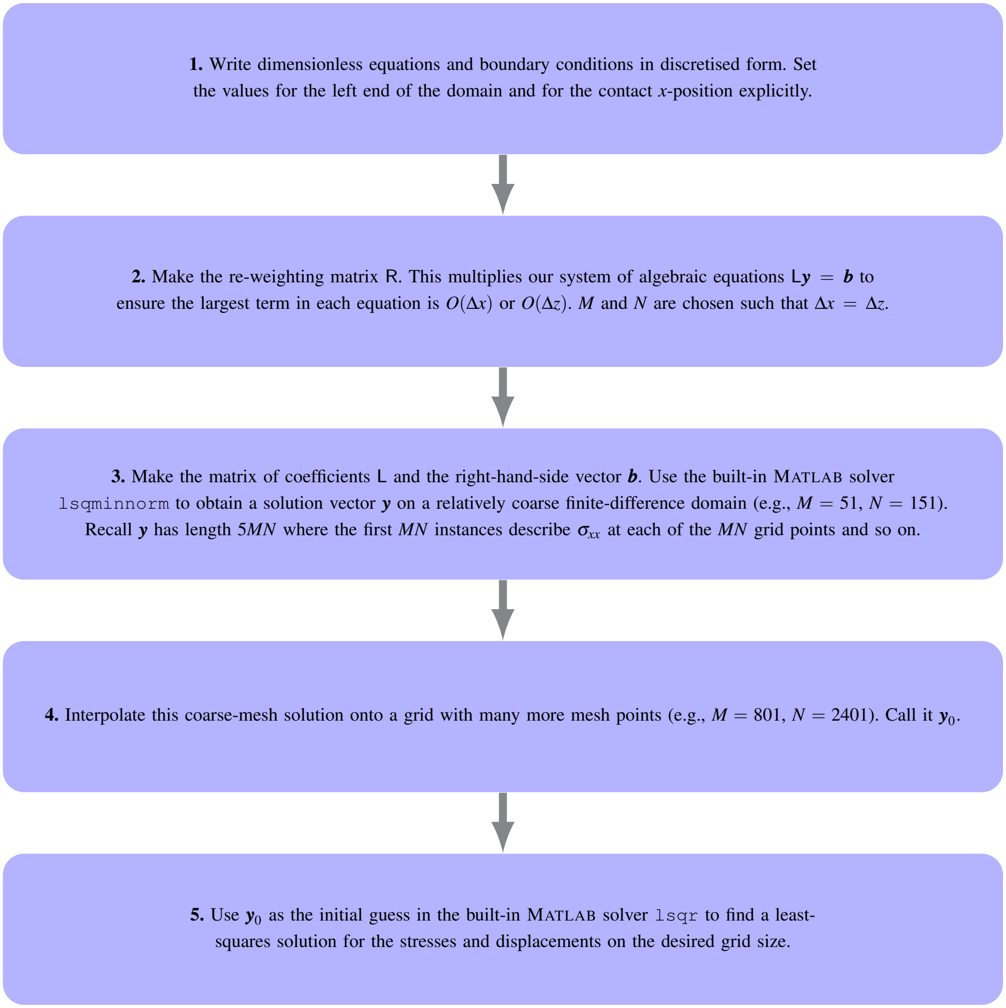

1. Write dimensionless equations and boundary conditions in discretised form. Set the values for the left end of the domain and for the contact x-position explicitly.

2. Make the re-weighting matrix R. This multiplies our system of algebraic equations $\mathsf{L}\boldsymbol{y} = \boldsymbol{b}$ to ensure the largest term in each equation is $O(\Delta x)$ or $O(\Delta z)$. M and N are chosen such that $\Delta x = \Delta z$.

3. Make the matrix of coefficients L and the right-hand-side vector $\boldsymbol{b}$. Use the built-in MATLAB solver `lsqminnorm` to obtain a solution vector $\boldsymbol{y}$ on a relatively coarse finite-difference domain (e.g., $M = 51$, $N = 151$). Recall $\boldsymbol{y}$ has length $5MN$ where the first MN instances describe σ_{xx} at each of the MN grid points and so on.

4. Interpolate this coarse-mesh solution onto a grid with many more mesh points (e.g., $M = 801$, $N = 2401$). Call it $\boldsymbol{y}_0$.

5. Use $\boldsymbol{y}_0$ as the initial guess in the built-in MATLAB solver `lsqr` to find a least-squares solution for the stresses and displacements on the desired grid size.

FIG. A.2. Infographic of the Model D solution process in MATLAB.

size to facilitate comparisons. Each downsized solution is subtracted from the solution at the preceding grid size. The maximum absolute difference across the domain is divided by the maximum absolute value of the larger-grid-size solution to give the normalised error. The normalised error is then plotted on a logarithmic scale. We see a decreasing trend in all quantities until the 1601×4801 grid size is used. For this convergence study, the correct contact x-position has been determined up to three decimal places (see Section A.3). We expect any further significant reductions in the normalised error in Figure A.3 to necessitate a more accurate contact x-position. The largest deviation in any stress or displacement quantity for the 801×2401 mesh solution is below 6% when comparing to a finer mesh (1601×4801). This error is sufficiently small, and therefore we take 801×2401 to be a sufficiently refined finite-difference grid size.

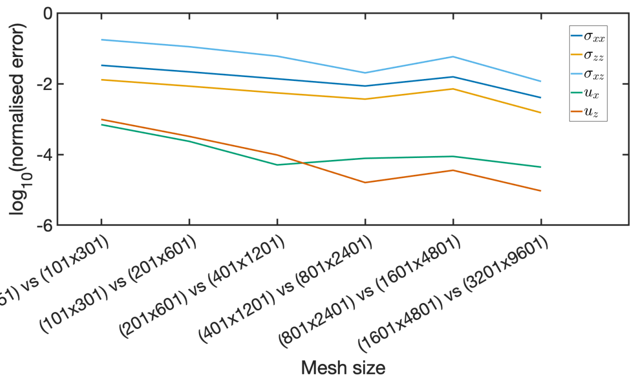

FIG. A.3. Plot of the logarithmic normalised error of the stresses and displacements for different finite-difference mesh-grid sizes with $x_c = 0.181$. For each stress or displacement quantity, the larger-grid-size solution is downsized to the preceding grid size to facilitate comparisons. Each downsized solution is subtracted from the solution at the preceding grid size. The maximum absolute difference across the domain is divided by the maximum absolute value of the larger-grid-size solution to give the normalised error. The correct contact x-position has been determined up to three decimal places.

A.3. *Determination of the contact point*

Recall that $x = x_c$ represents the x-position at which the roller and the sheet first come into contact. For Model D only, the contact position $x = x_c$ must be set manually (see step 2 in Figure A.2). Thus a criterion for choosing the correct x_c value is required. Correct determination of x_c is crucial as the boundary conditions change along the top surface of the sheet at $x = x_c$ (recall Figure 2 in the main text). We also recall that x_c is defined such that $x_c \geq 0$ where $x = 0$ is the x-position at which the roller and sheet would meet if the sheet did not deform at all before contacting the rollers. An x_c value of c corresponds to a contact $\hat{x}$-position of $\hat{x}_c = c\hat{h}_0$ in dimensional terms.

Since the norm $\|\mathsf{RL}\boldsymbol{y} - \mathsf{R}\boldsymbol{b}\|$ informs us about how well-satisfied the PDEs and boundary conditions are, and the prescription of x_c provides us with an extra degree of freedom in the problem, we hypothesise that the most correct value of x_c should minimise this norm. This hypothesis is tested for $0 \leq x_c \leq 1$ with a mesh of size 801×2401. This leads to a small range of contact points, $(0.175–0.2)$, giving similar small values of $\|\mathsf{RL}\boldsymbol{y} - \mathsf{R}\boldsymbol{b}\|$. To one decimal place, the contact x-position is thus $x_c = 0.2$. Further accuracy is desired so another criterion is put in place.

Before contact the surface stress is zero. As the roller smoothly contacts the sheet, we expect $\sigma_{zz}^{(0)}$ on the surface to decrease smoothly and monotonically to some negative value at the end of the elastic region. Figure A.4 shows the value of $\sigma_{zz}^{(0)}$ along the surface of the sheet in the entrance region for different values of x_c. We interpret values of x_c for which $\sigma_{zz}^{(0)}$ turns positive on the surface to be too small, as they correspond to material being pulled vertically upward to touch the roller. In Figure A.4 we can see this positive value of $\sigma_{zz}^{(0)}$ near the contact point in the $x_c = 0.175$ result. Similarly, we interpret values of x_c with a spike after the contact point, shown in the $x_c = 0.2$ result, to be too large. A careful parameter study yields a contact x-position of $x_c = 0.181$, to three decimal places, resulting in the monotonically decreasing $\sigma_{zz}^{(0)}$ result on the surface of the sheet in Figure A.4. The sharp corner at the contact point is not concerning as $\partial\sigma_{zz}^{(0)}/\partial x$ does not appear in the mathematical formulation of the problem. Model D thus predicts the contact point during a rolling process is $\hat{x} = 0.181\hat{h}_0$ past the

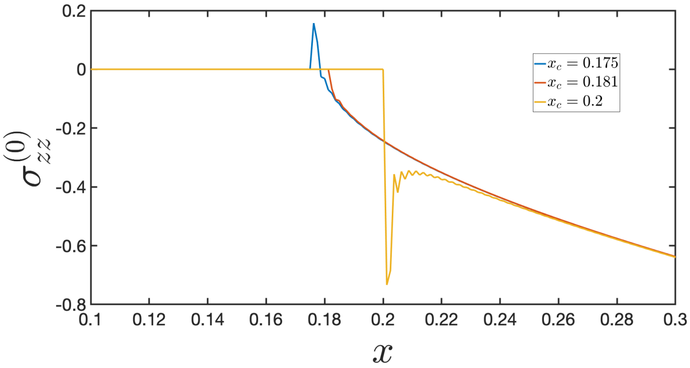

FIG. A.4. Dimensionless plot of $\sigma_{zz}^{(0)}$ on the surface of the sheet in Model D for different contact positions x_c. The positive spike near $x = x_c$ observed for the $x_c = 0.175$ result is an unrealistic artefact in the finite-difference solution and shows that this x_c value is too small to be the correct value for the contact position. The monotonically decreasing nature of the stress result for $x_c = 0.181$ shows that this is the most correct value for the contact position. The non-monotonic nature of the $x_c = 0.2$ result shows that this is too large to be the correct value for the contact position. (Colour online)

$\hat{x}$-position at which the roller and sheet would meet if the sheet did not deform at all before contacting the rollers.

A.4. *Model S solution process*

As stated at the beginning of this appendix, the finite-difference solution process for Model S is very similar to the Model D process. We point out the subtle differences here.

The original problem in Model S is on a domain $x \in (-\infty, x_t(z)]$, $z \in [0,1]$. This is mapped onto a simpler domain via the change of variables

$$\zeta = x - x_t(z), \qquad \phi = z, \tag{A.2}$$

so that derivatives are changed via

$$\frac{\partial}{\partial x} = \frac{\partial}{\partial \zeta}, \quad \frac{\partial}{\partial z} = \frac{\partial}{\partial \phi} - x_t'(z)\frac{\partial}{\partial \zeta}, \tag{A.3}$$

and the domain is simplified to $\zeta \in (-\infty, 0]$, $\phi \in [0,1]$.

Using the assumption (3.1) for x_t, and after taking the limit $\hat{k}/\hat{E} \to 0$ the leading-order problem to be solved numerically is

$$\frac{\partial \sigma_{xx}^{(0)}}{\partial \zeta} + \frac{\partial \sigma_{xz}^{(0)}}{\partial \phi} + 2x_0\phi \frac{\partial \sigma_{xz}^{(0)}}{\partial \zeta} = 0, \tag{A.4a}$$

$$\frac{\partial \sigma_{xz}^{(0)}}{\partial \zeta} + \frac{\partial \sigma_{zz}^{(0)}}{\partial \phi} + 2x_0\phi \frac{\partial \sigma_{zz}^{(0)}}{\partial \zeta} = 0, \tag{A.4b}$$

$$\frac{\partial u_x^{(0)}}{\partial \zeta} = (1+\nu)\left[(1-\nu)\sigma_{xx}^{(0)} - \nu\sigma_{zz}^{(0)}\right], \tag{A.4c}$$

$$\frac{\partial u_z^{(0)}}{\partial \phi} + 2x_0\phi\frac{\partial u_z^{(0)}}{\partial \zeta} = (1+\nu)\left[(1-\nu)\sigma_{zz}^{(0)} - \nu\sigma_{xx}^{(0)}\right], \tag{A.4d}$$

$$\frac{\partial u_x^{(0)}}{\partial \phi} + 2x_0\phi\frac{\partial u_x^{(0)}}{\partial \zeta} + \frac{\partial u_z^{(0)}}{\partial \zeta} = 2(1+\nu)\sigma_{xz}^{(0)}. \tag{A.4e}$$

The leading-order boundary conditions are

$$u_x^{(0)} = 0, \quad \sigma_{xz}^{(0)} = 0, \qquad \text{as } \zeta \to -\infty, \tag{A.5a}$$

$$\sigma_{xx}^{(0)} = \sigma_{zz}^{(0)} + 2 = \frac{\hat{T}_{\text{in}}}{\hat{h}_0\hat{k}}, \qquad \text{at } \zeta = 0, \tag{A.5b}$$

$$u_z^{(0)} = \sigma_{xz}^{(0)} = 0, \qquad \text{at } \phi = 0, \tag{A.5c}$$

$$\sigma_{xz}^{(0)} = \sigma_{zz}^{(0)} = 0, \qquad \text{at } \phi = 1. \tag{A.5d}$$

Practically, we truncate the semi-infinite domain at $\zeta = -3$ for numerical solution, in line with the procedure for Model D, and use the same mesh of size 801×2401 in Model S. Here, no contact x-position has to be chosen for Model S since we assume that the point $(x,z) = (0,1)$ is the top of the yielding boundary and the initial contact point (see Section 3 in the main text).